

$B_s \rightarrow D_s \ell \nu$ form factors for the full q^2 range from lattice QCD with nonperturbatively normalized currents

E. McLean,^{1,*} C. T. H. Davies^{1,†}, J. Koponen,² and A. T. Lyle³

(HPQCD collaboration)[‡]

¹*SUPA, School of Physics and Astronomy, University of Glasgow, Glasgow G12 8QQ, United Kingdom*

²*High Energy Accelerator Research Organisation (KEK), Tsukuba 305-0801, Japan*

³*INFN, Sezione di Roma Tor Vergata, Via della Ricerca Scientifica 1, 00133 Roma RM, Italy*



(Received 17 June 2019; accepted 3 April 2020; published 22 April 2020)

We present a lattice QCD determination of the $B_s \rightarrow D_s \ell \nu$ scalar and vector form factors over the full physical range of momentum transfer. The result is derived from correlation functions computed using the highly improved staggered quark (HISQ) formalism, on the second generation MILC gluon ensembles accounting for up, down, strange and charm contributions from the sea. We calculate correlation functions for three lattice spacing values and an array of unphysically light b -quark masses, and extrapolate to the physical value. Using the HISQ formalism for all quarks means that the lattice current coupling to the W can be renormalized nonperturbatively, giving a result free from perturbative matching errors for the first time. Our results are in agreement with, and more accurate than, previous determinations of these form factors. From the form factors we also determine the ratio of branching fractions that is sensitive to violation of lepton universality: $R(D_s) = \mathcal{B}(B_s \rightarrow D_s \tau \nu_\tau) / \mathcal{B}(B_s \rightarrow D_s \ell \nu_\ell)$, where ℓ is an electron or a muon. We find $R(D_s) = 0.2993(46)$, which is also more accurate than previous lattice QCD results. Combined with a future measurement of $R(D_s)$, this could supply a new test of the Standard Model. We also compare the dependence on heavy quark mass of our form factors to expectations from heavy quark effective theory.

DOI: [10.1103/PhysRevD.101.074513](https://doi.org/10.1103/PhysRevD.101.074513)

I. INTRODUCTION

The weak decay processes of mesons such as the B and B_s , containing b quarks, are a key potential source of insights into physics beyond the Standard Model (SM). Flavor-changing B decays have gained a lot of interest because of a number of related tensions between experimental measurements and SM predictions [1–19]. These tensions drive the need for improved theoretical calculations in the SM using methods and studying processes where we have good control of the uncertainties.

Lattice QCD is the method of choice for providing the hadronic input known as form factors that determine, up to a normalization factor, the differential branching fraction

for exclusive decay processes such $B \rightarrow D \ell \nu$ (we suppress all electric charge and particle-antiparticle labels here in referring to decay processes). The normalization factor that can then be extracted by comparison of theory with experiment is the Cabibbo-Kobayashi-Maskawa matrix element, in this case $|V_{cb}|$ [20–24]. Determination of $|V_{cb}|$ then feeds into constraints on new physics through, for example, tests of the unitarity triangle.

There has been a longstanding tension in determinations of $|V_{cb}|$ between *exclusive* (from $B \rightarrow D \ell \nu$ and $B \rightarrow D^* \ell \nu$ decays), and *inclusive* (from $B \rightarrow X_c \ell \nu$, where X_c is any charmed hadronic state) processes. The most accurate exclusive results came from studies of the $B \rightarrow D^* \ell \nu$ decay at zero recoil. It now seems likely that the uncertainties there were being underestimated because of the use of a very constrained parametrization in the extrapolation of the experimental $B \rightarrow D^*$ data to the zero recoil limit [25–28], but see also [29,30]. This underlines the importance in future of comparing theory and experiment across the full range of squared 4-momentum transfer (q^2) (a point emphasized for $D \rightarrow K$ in [31]). It also demonstrates the need for comparison of accurate results from multiple decay processes for a more complete picture. Improved

*e.mclean.1@research.gla.ac.uk

†christine.davies@glasgow.ac.uk

‡<http://www.physics.gla.ac.uk/HPQCD>

Published by the American Physical Society under the terms of the [Creative Commons Attribution 4.0 International license](https://creativecommons.org/licenses/by/4.0/). Further distribution of this work must maintain attribution to the author(s) and the published article's title, journal citation, and DOI. Funded by SCOAP³.

methods for producing the theoretical input to $|V_{cb}|_{\text{excl}}$, namely lattice QCD determinations of form factors, are clearly necessary.

Here we provide improved accuracy for the form factors for the $B_s \rightarrow D_s \ell \nu$ decay using a new lattice QCD method that covers the full q^2 range of the decay for the first time. Preliminary results appeared in [32]. The $B_s \rightarrow D_s$ form factors are more attractive than $B \rightarrow D$ for a first calculation to test methodology. They are numerically faster to compute and have higher statistical accuracy and smaller finite-volume effects because no valence u/d quarks are present. Chiral perturbation theory [33] expects that the $B \rightarrow D$ form factors should be relatively insensitive to the spectator quark mass and hence should be very similar between $B_s \rightarrow D_s$ and $B \rightarrow D$. This is confirmed at the 5% level by lattice QCD calculations [34,35]. Hence improved calculations of $B_s \rightarrow D_s$ form factors can also offer information on $B \rightarrow D$.

Given an experimental determination, the $B_s \rightarrow D_s \ell \nu$ decay can supply a new method for precisely determining the Cabibbo-Kobayashi-Maskawa (CKM) element $|V_{cb}|$. It can also supply a new test of the SM through quantities sensitive to lepton universality violation. We give the SM result for $R(D_s) = \mathcal{B}(B_s \rightarrow D_s \tau \nu_\tau) / \mathcal{B}(B_s \rightarrow D_s l \nu_l)$, where $l = e$ or μ . An experimental value for comparison to this would help to clarify the tension found between the SM and experiment in the related ratios $R(D^{(*)}) = \mathcal{B}(B \rightarrow D^{(*)} \tau \nu_\tau) / \mathcal{B}(B \rightarrow D^{(*)} l \nu_l)$ [36] (see also a preliminary new analysis by Belle [37]).

Three lattice QCD calculations of $B_{(s)} \rightarrow D_{(s)}$ form factors have already been performed. The FNAL/MILC collaboration [22,34] used the Fermilab action for the b and c quarks and the asqtad action for the light quarks on MILC gluon field ensembles that include $2 + 1$ flavors of asqtad sea quarks. On the same gluon field ensembles the HPQCD collaboration has calculated the form factors using non-relativistic QCD (NRQCD) for the valence b and the highly improved staggered quark (HISQ) action for the other valence quarks [23,35]. A further calculation has been done using maximally twisted Wilson quarks on $n_f = 2$ gluon field ensembles [38]. Preliminary results using domain-wall quarks are given in [39].

A considerable limitation in the FNAL/MILC and HPQCD/NRQCD studies is the requirement for normalization of the lattice QCD $b \rightarrow c$ current. The matching between this current and that of continuum QCD is done in lattice QCD perturbation theory through $\mathcal{O}(\alpha_s)$, giving a $\mathcal{O}(\alpha_s^2)$ systematic error which can be sizeable. Systematic errors coming from the truncation of the nonrelativistic expansion of the current are also a problem. In the Fermilab formalism the missing terms become $\mathcal{O}(\alpha_s a)$ discretization effects on fine enough lattices; in the NRQCD formalism they mix discretization effects and $\mathcal{O}(\alpha_s/m_b)$ (where m_b is the b quark mass) relativistic corrections. Here we dispense with both of these problems by using a relativistic

formalism with absolutely normalized lattice QCD currents.

Another limitation present in each of the previous studies is that the lattice QCD results are limited to a region of high q^2 , close to zero recoil. The reason for this is mainly to avoid large statistical errors. The signal/noise degrades exponentially as the spatial momentum of the meson in the final state grows. For b quark decays the maximum spatial momentum of the final state meson can be large (tending to $m_B/2$ for light mesons, where m_B is the B meson mass). Systematic errors from missing discretization (and relativistic) corrections also grow away from zero recoil. This is particularly problematic if discretization effects are $\mathcal{O}(a)$ as above and relatively coarse lattices are used (to reduce numerical cost). Working close to zero recoil means that the lattice results then have to be extrapolated from the high q^2 region into the rest of the physical q^2 range. Here we also overcome this problem by working with a highly improved quark action in which even $\mathcal{O}(a^2)$ errors have been eliminated at tree-level [40]. We cover a range of values of the lattice spacing that includes very fine lattices and include results from lighter than physical b quarks and this enables us to cover the full q^2 range in our lattice calculation.

We perform our calculation on the second-generation MILC gluon ensembles [41], including effects from $2 + 1 + 1$ flavors in the sea using the HISQ action [40]. We also use the HISQ action for all valence quarks. Our calculation employs HPQCD's *heavy-HISQ* approach. In this we obtain lattice results at a number of unphysically light masses for the b (we refer to this generically as the *heavy quark* h), reaching the b quark mass on the finest lattices. This allows us to perform a combined fit in m_h and lattice spacing that we can evaluate in the continuum limit at $m_h = m_b$ [and as a function of m_h to compare, for example, to expectations from heavy quark effective theory (HQET)]. By using only HISQ quarks, we can normalize all the lattice currents fully nonperturbatively and avoid systematic errors from current matching.

This calculation adds to a growing number of successful demonstrations of the heavy-HISQ approach. The method was developed for determination of the b quark mass, B meson masses and decay constants [42–44] and is now also being used by other groups for these calculations [45,46]. A proof-of-principle application of heavy-HISQ to form factors was given for $B_c \rightarrow \eta_c$ and $B_c \rightarrow J/\psi$ in [47,48], covering the full q^2 range for these decays and this work builds on those results. The $B_s \rightarrow D_s^*$ axial form factor at zero recoil was calculated using heavy-HISQ in [49].

This article is structured in the following way: Section II lays out our lattice QCD approach to calculating the form factors and then Sec. III presents our results, along with several consistency checks and our determination of $R(D_s)$. We also give curves showing the heavy-quark mass dependence of some features of the form factors that can

be compared to HQET. For those simply hoping to use our calculated $B_s \rightarrow D_s$ form factors, Appendix A gives the parameters and covariance matrix required to reconstruct them.

II. CALCULATION DETAILS

A. Form factors

In this section we specify our notation for the form factors and matrix elements. The differential decay rate for $B_s \rightarrow D_s \ell \nu$ decays is given in the SM by

$$\begin{aligned} \frac{d\Gamma}{dq^2} &= \eta_{\text{EW}} \frac{G_F^2 |V_{cb}|^2}{24\pi^3 M_{B_s}^2} \left(1 - \frac{m_\ell^2}{q^2}\right)^2 |\mathbf{p}_{D_s}| \\ &\times \left[\left(1 + \frac{m_\ell^2}{2q^2}\right) M_{B_s}^2 |\mathbf{p}_{D_s}|^2 f_+^{s2}(q^2) \right. \\ &\left. + \frac{3m_\ell^2}{8q^2} (M_{B_s}^2 - M_{D_s}^2)^2 f_0^{s2}(q^2) \right] \end{aligned} \quad (1)$$

where m_ℓ is the mass of the lepton, η_{EW} is the electroweak correction, $q^2 = (p_{B_s} - p_{D_s})^2$ is the momentum transfer and $f_0^s(q^2)$, $f_+^s(q^2)$ are the scalar and vector form factors that parametrize the fact that the decay process involves hadrons. We use superscript “s” to denote the strange spectator valence quark. The allowed range of q^2 values if the final states are on-shell is

$$m_\ell^2 \leq q^2 \leq (M_{B_s} - M_{D_s})^2. \quad (2)$$

The form factors are determined from matrix elements of the electroweak current between B_s and D_s states, $\langle D_s | (V - A)^\mu | B_s \rangle$ where $V^\mu = \bar{b} \gamma^\mu c$ is the vector component and $A^\mu = \bar{b} \gamma^5 \gamma^\mu c$ is the axial vector component. In a pseudoscalar-to-pseudoscalar amplitude, only V^μ contributes, since $\langle D_s | A^\mu | B_s \rangle$ does not satisfy the parity invariance of QCD. In terms of form factors, the vector current matrix element is given by

$$\begin{aligned} \langle D_s | V^\mu | B_s \rangle &= f_+^s(q^2) \left[p_{B_s}^\mu + p_{D_s}^\mu - \frac{M_{B_s}^2 - M_{D_s}^2}{q^2} q^\mu \right] \\ &+ f_0^s(q^2) \frac{M_{B_s}^2 - M_{D_s}^2}{q^2} q^\mu. \end{aligned} \quad (3)$$

Analyticity of this matrix element demands that

$$f_+^s(0) = f_0^s(0). \quad (4)$$

Via the partially conserved vector current relation (PCVC), the form factor $f_0^s(q^2)$ is also directly related to the matrix element of the scalar current $S = \bar{b}c$;

$$(m_b - m_c) \langle D_s | S | B_s \rangle = (M_{B_s}^2 - M_{D_s}^2) f_0^s(q^2). \quad (5)$$

In our calculation we determine the form factors by computing matrix elements of the temporal vector current V^0 and the scalar current S . The form factors can be extracted from this combination using expressions derived from Eqs. (3) and (5) (once the currents have the correct continuum normalization—see Sec. IID):

$$\begin{aligned} f_0^s(q^2) &= \frac{m_b - m_c}{M_{B_s}^2 - M_{D_s}^2} \langle D_s | S | B_s \rangle, \\ f_+^s(q^2) &= \frac{1}{2M_{B_s}} \frac{\delta^M \langle D_s | S | B_s \rangle - q^2 \langle D_s | V^0 | B_s \rangle}{\mathbf{p}_{D_s}^2}, \\ (\delta^M &= (m_b - m_c)(M_{B_s} - E_{D_s})). \end{aligned} \quad (6)$$

Our goal is to compute $f_0^s(q^2)$ and $f_+^s(q^2)$ throughout the range of q^2 values $0 \leq q^2 \leq (M_{B_s} - M_{D_s})^2 \equiv q_{\text{max}}^2$. We extend the range to $q^2 = 0$ in order to take advantage of the constraint from Eq. (4).

B. Lattice calculation

This calculation closely follows the approach employed in our calculation of the $B_s \rightarrow D_s^*$ axial form factor at zero recoil [49]. Here, however, we must give spatial momentum to the charm quark in the final state so that we can cover the full q^2 range of the decay.

TABLE I. Parameters for gluon field ensembles [41,50]. a is the lattice spacing, determined from the Wilson flow parameter [52]. The physical value of w_0 was determined using f_π to be 0.1715(9) fm in [53]. This allows the determination of w_0/a on individual sets of gluon field configurations to be converted into a value of a . These are given in column 3 with the uncertainty quoted being the statistical uncertainty in w_0/a on that ensemble [54–56]. There is an additional uncertainty in a , correlated across all ensembles, from the physical value of w_0 . N_x is the spatial extent and N_t the temporal extent of the lattice in lattice units. Light ($m_u = m_d$), strange and charm quarks are included in the sea, their masses are given in columns 5–7.

| Set | Handle | a/fm | $N_x^3 \times N_t$ | am_{l0} | am_{s0} | am_{c0} |
|-----|----------------------|---------------|--------------------|-----------|-----------|-----------|
| 1 | <i>Fine</i> | 0.09023(48) | $32^3 \times 96$ | 0.0074 | 0.037 | 0.440 |
| 2 | <i>Fine-physical</i> | 0.08787(46) | $64^3 \times 96$ | 0.0012 | 0.0363 | 0.432 |
| 3 | <i>Superfine</i> | 0.05922(33) | $48^3 \times 144$ | 0.0048 | 0.024 | 0.286 |
| 4 | <i>Ultrafine</i> | 0.04406(27) | $64^3 \times 192$ | 0.00316 | 0.0158 | 0.188 |

The gluon field configurations used in this calculation were generated by the MILC collaboration [41,50]. The relevant parameters for the specific ensembles we use are given in Table I. The gluon fields are generated using a Symanzik-improved gluon action with coefficients matched to continuum QCD through $\mathcal{O}(\alpha_s a^2, n_f \alpha_s a^2)$ [51]. The gluon fields include the effect of $2 + 1 + 1$ flavors of quarks in the sea (u, d, s, c , where $m_{u0} = m_{d0} \equiv m_{l0}$) using the HISQ action [40]. In three of the four ensembles (sets 1, 3 and 4), the bare light quark mass is set to $m_{l0}/m_{s0} = 0.2$. The fact that the m_{l0} value is unphysically high is expected to have only a small effect on the form factors here, since we have no valence light quarks. We quantify this small effect by including a fourth ensemble (set 2) with roughly physical m_{l0} .

We use a number of different masses for the valence heavy quark am_{h0}^{val} . This allows us to resolve the dependence of the form factors on the heavy quark mass, so that a fit in m_h can be performed and the results of the fit evaluated at $m_h = m_b$. With a heavy quark mass varying both on a given ensemble and between ensembles, we can resolve both the discretization effects that grow with large ($am_{h0}^{\text{val}} \gtrsim 1$) masses and the physical dependence of the continuum form factors on m_h . Using unphysically light h -quarks also reduces the q^2 range, meaning that we can obtain lattice results across the full range while the statistical noise remains under control.

Staggered quarks have no spin degrees of freedom. Spin-parity quantum numbers are accounted for by construction

of appropriate fermion bilinears and including an appropriate space-time dependent phase with each operator in the path integral. We categorize these phases according to the standard *spin-taste* notation, $(\gamma_n \otimes \gamma_s)$, where γ_n is the spin structure of the operator in the continuum limit, and γ_s is the ‘‘taste’’ structure which accounts for the multiple possible copies of the operator constructed from staggered quark fields.

We have designed this calculation to use only local operators (combining fields at the same space-time point and having $(\gamma_n \otimes \gamma_n)$ spin-taste) for the calculation of the current matrix elements that we require. This is an advantage since point-split operators can lead to noisier correlation functions. The spin-taste operators we use are: scalar ($1 \otimes 1$), pseudoscalar ($\gamma^5 \otimes \gamma^5$), vector ($\gamma^\mu \otimes \gamma^\mu$), and temporal axial-vector ($\gamma^0 \gamma^5 \otimes \gamma^0 \gamma^5$).

We compute a number of correlation functions on the ensembles detailed in Table I. Valence quark masses, momenta and other inputs to the calculation are given in Table II. We use random wall sources to generate all staggered propagators from the source since this gives improved statistical errors [57]. First we compute two-point correlation functions between meson eigenstates of momentum $a\mathbf{p}$,

$$C_M^{a\mathbf{p}}(t) = \frac{1}{N_{\text{taste}}} \langle \tilde{\Phi}_M(\mathbf{p}, t) \tilde{\Phi}_M^\dagger(\mathbf{p}, 0) \rangle,$$

$$\tilde{\Phi}_M(\mathbf{p}, t) = \sum_{\mathbf{x}} e^{-i\mathbf{p}\cdot\mathbf{x}} \bar{q}(\mathbf{x}, t) \Gamma q'(\mathbf{x}, t), \quad (7)$$

TABLE II. Computational details. Columns 2 and 3 give the s and c valence quark masses in lattice units, which were tuned in [54]. In column 4 we give the heavy quark masses that we used in lattice units. We use a number of heavy quark masses to enable the heavy-quark mass dependence to be determined in our fit. Column 5 gives the ratio of heavy and charm valence quark masses, to give physical intuition for the heavy masses we use. The physical value for this is given by 4.528(54) (for $N_f = 4$) [54]. Column 6 gives the absolute value of the spatial momentum (in lattice units) given to the D_s meson using a momentum twist on the charm quark propagator. These values are chosen with the following rationale: when only two values are given, these correspond to the $q^2 = 0$ and q_{max}^2 points (except on the fine-physical ensemble, where we use the points q_{max}^2 and $q_{\text{max}}^2/2$); when three values are given, the momenta correspond to $q^2 = 0$, $q^2 = q_{\text{max}}^2/2$, and q_{max}^2 ; when four values are given, these are points corresponding to q_{max}^2 , $3q_{\text{max}}^2/4$, $q_{\text{max}}^2/2$, $q_{\text{max}}^2/4$ and $q^2 = 0$. We used twisted momenta in the (1,1,1) direction to minimize discretization effects. Column 7 gives the number of gluon field configurations used for that ensemble, n_{cfg} , and the number of different time sources used per configuration to increase statistics, n_{src} . Column 8 gives the temporal separations between source and sink, T , of the three-point correlation functions computed on each ensemble. Columns 9-13 give the t_{cut} values chosen for the corresponding correlator fits (see Sec. II C); η_q denotes the correlators for η_s , η_c and η_h mesons and J denotes all 3-point correlators. Column 8 gives the t_{cut} used for both tastes of H_s meson that we use.

| Set | am_{s0}^{val} | am_{c0}^{val} | am_{h0}^{val} | $am_{h0}^{\text{val}}/am_{c0}^{\text{val}}$ | $ a\mathbf{p}_{D_s} $ | $n_{\text{cfg}} \times n_{\text{src}}$ | T | t_{cut} : | H_s | D_s | H_c | η_q | J |
|-----|------------------------|------------------------|------------------------|---|------------------------|--|------------|--------------------|-------|-------|-------|----------|-----|
| 1 | 0.0376 | 0.45 | 0.5 | 1.11 | 0, 0.056 | 986 × 8 | 14, 17, 20 | | 2 | 2 | 2 | 2 | 2 |
| | | | 0.65 | 1.44 | 0, 0.142, 0.201 | | | | | | | | |
| | | | 0.8 | 1.78 | 0, 0.227, 0.323 | | | | | | | | |
| 2 | 0.036 | 0.433 | 0.5 | 1.16 | 0, 0.0279 | 286 × 4 | 14, 17, 20 | | 4 | 4 | 5 | 4 | 2 |
| | | | 0.8 | 1.85 | 0, 0.162 | | | | | | | | |
| 3 | 0.0234 | 0.274 | 0.427 | 1.56 | 0, 0.113, 0.161 | 250 × 8 | 22, 25, 28 | | 5 | 5 | 10 | 5 | 4 |
| | | | 0.525 | 1.92 | 0, 0.161, 0.244 | | | | | | | | |
| | | | 0.65 | 2.37 | 0, 0.244, 0.338 | | | | | | | | |
| | | | 0.8 | 2.92 | 0, 0.338, 0.438 | | | | | | | | |
| 4 | 0.0165 | 0.194 | 0.5 | 2.58 | 0, 0.202, 0.281 | 237 × 4 | 31, 36, 41 | | 2 | 2 | 8 | 2 | 4 |
| | | | 0.65 | 3.35 | 0, 0.202, 0.281, 0.382 | | | | | | | | |
| | | | 0.8 | 4.12 | 0, 0.281, 0.382, 0.473 | | | | | | | | |

where $\langle \rangle$ represents a functional integral over all fields, q, q' are valence quark fields of the flavors the M meson is charged under, Γ is the spin-taste structure of M and the division by the number of tastes is required to normalize closed loops made from staggered quarks [40]. We compute these correlation functions for all t values, i.e., $0 \leq t \leq N_t$.

We compute correlation functions for a heavy-strange pseudoscalar, H_s , with spin-taste structure $(\gamma^5 \otimes \gamma^5)$, at rest. In terms of staggered quark propagators this takes the form

$$C_{H_s}(t) = \frac{1}{4} \sum_{\mathbf{x}, \mathbf{y}} \langle \text{Tr}[g_h(x, y) g_s^\dagger(x, y)] \rangle, \quad (8)$$

where $g_q(x, y)$ is a staggered propagator for flavor q , and the trace is over color. Here $x_0 = 0$ and $y_0 = t$, and the sum is over spatial sites labelled \mathbf{x}, \mathbf{y} . We also compute correlators for a charm-strange pseudoscalar meson D_s , with structure $(\gamma^5 \otimes \gamma^5)$. For these correlators we need both zero and non-zero spatial momentum. Nonzero spatial momentum is given to the D_s by imposing twisted boundary conditions on the gluon fields when computing the charm quark propagators [58]. Then

$$C_{D_s}^{a\mathbf{p}}(t) = \frac{1}{4} \sum_{\mathbf{x}, \mathbf{y}} \langle \text{Tr}[g_c^\theta(x, y) g_s^\dagger(x, y)] \rangle, \quad (9)$$

where $g_q^\theta(x, y)$ denotes a propagator with momentum twist θ . We compute these correlation functions using several different twists to produce the range of momenta given in Table II. We design the c propagators to have momentum $a\mathbf{p} = |a\mathbf{p}|(1, 1, 1)$, by imposing a twist $\theta = N_x |a\mathbf{p}| / \pi \sqrt{3}$ in each spatial direction.

Necessary for extracting the vector current matrix element, we also compute correlation functions for a non-goldstone pseudoscalar heavy-strange mesons at rest, denoted \hat{H}_s . This has spin-taste structure $(\gamma^0 \gamma^5 \otimes \gamma^0 \gamma^5)$. \hat{H}_s correlators are computed using

$$C_{\hat{H}_s}(t) = \frac{1}{4} \sum_{\mathbf{x}, \mathbf{y}} \langle (-1)^{\bar{x}_0 + \bar{y}_0} \text{Tr}[g_h(x, y) g_s^\dagger(x, y)] \rangle, \quad (10)$$

where we use the notation $\bar{z}_\mu = \sum_{\nu \neq \mu} z_\nu$.

We also compute correlators for H_c mesons, heavy-charmed pseudoscalars, using the same form as those for H_s , Equation (8). These are used to find H_c decay constants, which are useful in some of our continuum and m_h fits. In our fits to heavy-quark mass dependence we will use the mass of the heavy-heavy pseudoscalar meson, η_h as a physical proxy for the quark mass. To quantify mistuning of the charm and strange quark masses, we also require masses for η_c and η_s mesons, identical to η_h with h replaced c and s quarks respectively. We compute

correlators for each of these at rest, using a spin-taste structure $(\gamma^5 \otimes \gamma^5)$, taking the same form as those of the H_s , Equation (8). Note that all of the η mesons discussed here are artificially forbidden to annihilate in our lattice QCD calculation. We expect this to have negligible effect, for the purposes of this calculation, on the masses of the η_c and the η_b [54]; the η_s is an unphysical meson that can be defined in this limit in a lattice QCD calculation and is convenient for tuning the s quark mass [53,59].

Three-point correlation functions are needed to allow determination of the current matrix elements for $B_s \rightarrow D_s$ decay. We require two sets of such correlation functions, one with a scalar and one with a temporal vector current insertion. The first takes the form

$$C_S^{a\mathbf{p}D_s}(t, T) = \frac{1}{N_{\text{taste}}} \sum_{\mathbf{y}} \langle \tilde{\Phi}_{D_s}(\mathbf{p}, T) S(\mathbf{y}, t) \tilde{\Phi}_{H_s}(\mathbf{0}, 0) \rangle, \quad (11)$$

$$S(\mathbf{y}, t) = \bar{c}(\mathbf{y}, t) h(\mathbf{y}, t).$$

In terms of the staggered quark formalism, both the H_s source and D_s sink are given structure $(\gamma^5 \otimes \gamma^5)$, and the current insertion $(1 \otimes 1)$. We combine staggered propagators to construct these correlation functions as:

$$C_S^{a\mathbf{p}D_s}(t, T) = \frac{1}{4} \sum_{\mathbf{x}, \mathbf{y}, \mathbf{z}} \langle \text{Tr}[g_h(x, y) g_c^\theta(y, z) g_s^\dagger(x, z)] \rangle, \quad (12)$$

where we fix $x_0 = 0, y_0 = t$ and $z_0 = T$, and once again the charm propagator is given the appropriate twist θ . We compute these correlation functions for all t values within $0 \leq t \leq T$, using 3 T values to make sure that excited state effects are accounted for. The T values vary with lattice spacing to give approximately the same physical range and always include both even and odd values. The values are given in Table II.

The three-point correlation function with temporal vector current insertion is given by

$$C_{V^0}^{a\mathbf{p}D_s}(t, T) = \frac{1}{N_{\text{taste}}} \sum_{\mathbf{y}} \langle \tilde{\Phi}_{D_s}(\mathbf{p}, T) V^0(\mathbf{y}, t) \tilde{\Phi}_{\hat{H}_s}(\mathbf{0}, 0) \rangle, \quad (13)$$

$$V^0(\mathbf{y}, t) = \bar{c}(\mathbf{y}, t) \gamma^0 h(\mathbf{y}, t).$$

This is generated using spin-taste $(\gamma^0 \gamma^5 \otimes \gamma^0 \gamma^5)$ at the \hat{H}_s source, $(\gamma^5 \otimes \gamma^5)$ at the D_s sink, and $(\gamma^0 \otimes \gamma^0)$ at the current insertion. To achieve this we compute

$$C_{V^0}^{a\mathbf{p}D_s}(t, T) = \frac{1}{4} \sum_{\mathbf{x}, \mathbf{y}, \mathbf{z}} \langle (-1)^{\bar{x}_0 + \bar{y}_0} \times \text{Tr}[g_h(x, y) g_c^\theta(y, z) g_s^\dagger(x, z)] \rangle. \quad (14)$$

The non-goldstone \hat{H}_s is required here to ensure that taste cancels in the correlation function. The difference between

the \hat{H}_s and the H_s , for example in their masses, is generated by taste-exchange discretization effects. In practice it is very small for heavy mesons [40], being suppressed by the heavy meson mass.

C. Analysis of correlation functions

We now describe our simultaneous multiexponential fits to the correlation functions using a standard Bayesian approach [60,61]. The parameters that we wish to determine are ground-state energies, two-point amplitudes and ground-state to ground-state matrix elements. Our correlation functions, however, are contaminated by contributions from excited states. These excited states must be included in our fits so that the systematic error on the ground-state parameters from the presence of the excited states is fully taken into account. Multiexponential fits are then mandatory, guided by Bayesian priors for the parameters, discussed below. To reduce the number of exponentials needed by the fits, we drop values of the correlation functions when they are within t_{cut} of the endpoints (where excited states contribute most). We use values of t_{cut} varying from 2 to 10 throughout the correlator fits; these values are given in Table II. We take results from fits using 5 exponentials ($N_{\text{exp}} = 5$ in the fit forms below), where good χ^2 values are obtained and the ground-state parameters and their uncertainties have stabilized.

Two-point correlation functions are fit to the form

$$C_M(t)|_{\text{fit}} = \sum_n^{N_{\text{exp}}} (|a_n^M|^2 f(E_n^M, t) - (-1)^t |a_n^{M,o}|^2 f(E_n^{M,o}, t)), \quad (15)$$

where

$$f(E, t) = (e^{-Et} + e^{-E(N_t-t)}), \quad (16)$$

and $E_n^{M,(o)}$, $a_n^{M,(o)}$ are fit parameters. The second term in Eq. (15) accounts for the opposite-parity states that arise from the staggered quark time doublers and are known as *oscillating states* (see Appendix G of [40]). These oscillating states do not appear when M is a Goldstone-taste pseudoscalar with a quark and antiquark of the same mass, so in the $M = \eta_h, \eta_c$, and η_s cases the second term is not required.

Figure 1 shows the quality of our results. We plot effective energies and amplitudes for the D_s and H_s mesons on the fine ensemble. For the effective energy $E_{\text{eff}}(t)$ we use

$$E_{\text{eff}}(t) = \frac{1}{2} \cosh^{-1} \left(\frac{C(t+2) + C(t-2)}{2C(t)} \right) \quad (17)$$

where $C(t)$ is defined in Eqs. (8) and (9). By comparing $C(t)$ to $C(t+2)$ and $C(t-2)$, we avoid contamination by the oscillating states. Similarly an effective amplitude can be computed according to

$$a_{\text{eff}}(t) = \sqrt{C(t)/f(E_{\text{eff}}(t), t)}. \quad (18)$$

As can be seen from Fig. 1, these quantities agree well with the results for the ground-state energies and amplitudes found from our multiexponential Bayesian fits.

For the three-point correlation functions we use the fit form

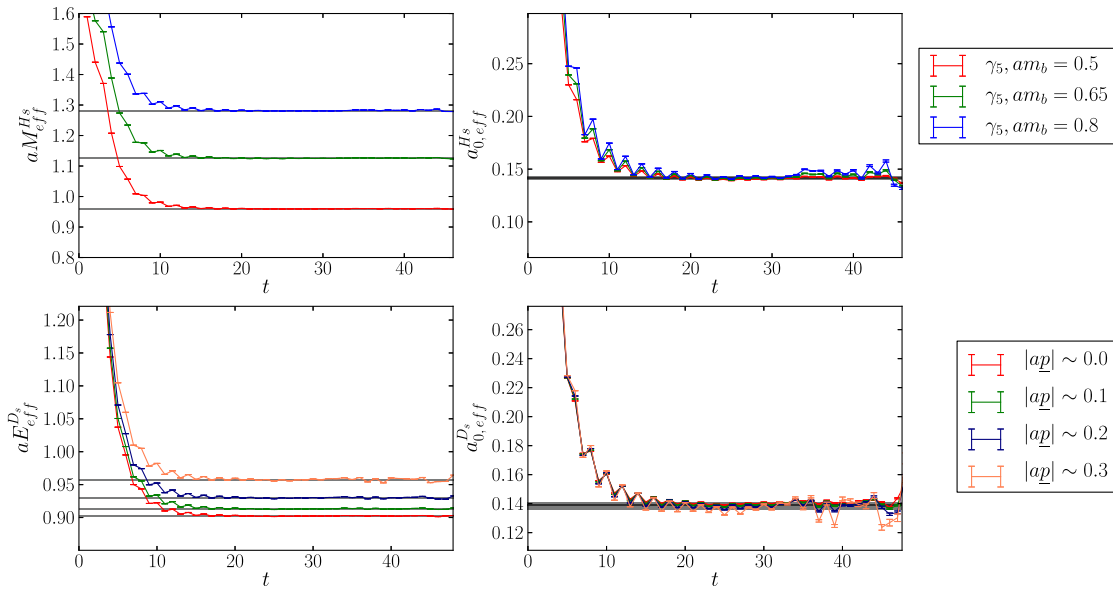


FIG. 1. Effective energies and amplitudes, defined from Eqs. (17) and (18) on the fine ensemble. Grey bands show the fit result for the ground-state energies and amplitudes including their uncertainty. The fit used the correlator data on time slices between $t = 2$ and $t = N_t - 2$.

TABLE III. Parameters determined from our correlation function fits. The decay constant af_{H_c} is extracted from the amplitude obtained via Eqs. (20) and (21). D_s energies at non-zero spatial momentum are given in Table IV.

| Set | am_h^{val} | aM_{H_s} | aM_{D_s} | aM_{H_c} | af_{H_c} | aM_{η_h} | aM_{η_c} | aM_{η_s} |
|-----|---------------------|-------------|--------------|--------------|--------------|---------------|---------------|---------------|
| 1 | 0.5 | 0.95971(12) | 0.90217(11) | 1.419515(41) | 0.186299(70) | 1.471675(38) | 1.367014(40) | 0.313886(75) |
| | 0.65 | 1.12507(18) | | 1.573302(40) | 0.197220(77) | 1.775155(34) | | |
| | 0.8 | 1.28129(19) | | 1.721226(39) | 0.207068(78) | 2.064153(30) | | |
| 2 | 0.5 | 0.95446(13) | 0.87715(11) | 1.400025(26) | 0.183482(46) | 1.470095(25) | 1.329291(27) | 0.304826(52) |
| | 0.8 | 1.27560(24) | | 1.702438(24) | 0.203382(50) | 2.062957(19) | | |
| 3 | 0.427 | 0.77443(17) | 0.59151(11) | 1.067224(46) | 0.126564(70) | 1.233585(41) | 0.896806(48) | 0.207073(96) |
| | 0.525 | 0.88470(21) | | 1.172556(46) | 0.130182(72) | 1.439515(37) | | |
| | 0.65 | 1.01973(28) | | 1.303144(46) | 0.133684(75) | 1.693895(33) | | |
| | 0.8 | 1.17436(40) | | 1.454205(46) | 0.137277(79) | 1.987540(30) | | |
| 4 | 0.5 | 0.80235(19) | 0.439899(86) | 1.011679(25) | 0.099031(45) | 1.342747(27) | 0.666754(39) | 0.153827(77) |
| | 0.65 | 0.96344(27) | | 1.169780(26) | 0.100598(49) | 1.650264(23) | | |
| | 0.8 | 1.11728(35) | | 1.321660(28) | 0.101765(54) | 1.945763(21) | | |

$$\begin{aligned}
 C_J(t, T)|_{\text{fit}} &= \sum_{k,j=0}^{N_{\text{exp}} \cdot N_{\text{exp}}} (a_j^{H_s} J_{jk}^{nn} a_k^{D_s} f(E_n^{H_s}, t) f(E_n^{D_s}, T-t) \\
 &+ a_j^{H_{s,o}} J_{jk}^{\text{on}} a_k^{D_s} (-1)^t f(E_n^{H_{s,o}}, t) f(E_n^{D_s}, T-t) \\
 &+ a_j^{H_s} J_{jk}^{\text{no}} a_k^{D_{s,o}} (-1)^{T-t} f(E_n^{H_s}, t) f(E_n^{D_{s,o}}, T-t) \\
 &+ a_j^{H_{s,o}} J_{jk}^{\text{oo}} a_k^{D_{s,o}} (-1)^T f(E_n^{H_{s,o}}, t) f(E_n^{D_{s,o}}, T-t)). \quad (19)
 \end{aligned}$$

This includes fit parameters common to the fits of H_s (when $J = S$), \hat{H}_s (when $J = V_0$) and D_s two-point correlators, along with new fit parameters J_{jk} that are related to the current matrix elements. We perform a single simultaneous fit containing each correlator computed ($C_{H_s}, C_{\hat{H}_s}, C_{D_s}, C_{\eta_h}, C_{\eta_c}, C_{\eta_s}, C_{H_c}, C_S, C_{V_0}$) at every am_h and every $|a\mathbf{p}_{D_s}|$, for each ensemble.

These simultaneous fits are very large and this causes problems for the covariance matrix which must be inverted to determine χ^2 . We take two steps toward mitigating this. The first is to impose an svd (singular value decomposition) cut c_{svd} . This replaces any eigenvalue of the covariance matrix smaller than $c_{\text{svd}}x$ with $c_{\text{svd}}x$, where x is the largest eigenvalue of the matrix.¹ The small eigenvalues are driven to zero if the statistics available are not high enough [62]. The application of the svd cut makes the matrix less singular, and can be considered a conservative move since the only possible effect on the error of the final results is to inflate them. An appropriate value for c_{svd} is found by comparing estimates of covariance matrix eigenvalues between different bootstrap samples of the data using the Corrfitter package [61]. The resulting c_{svd} varies between ensembles since it depends on the statistical

¹To give an example for context, the largest eigenvalue in the data from the fine ensemble is ~ 700 .

quality of the dataset, but we find them to be of order 10^{-3} . For more details of this approach, see Appendix D of [62].

The other step we take toward a stable fit is employing a chained-fitting approach. We first perform an array of smaller fits, each fitting the correlators relevant only to one m_h and one $|a\mathbf{p}_{D_s}|$ value. In the case of set 4, for example, this results in 11 separate fits. Then, a full simultaneous fit of all of the correlators is carried out, using as priors the results of the smaller fits. This both speeds up the full fit and improves stability of the results.

The priors for the fits were set up as follows. We set gaussian priors for the parameters J_{jk} , and log-normal priors for amplitudes a_i^M , ground-state energies E_0^M , and excited-state energy differences $E_{i+1}^M - E_i^M$. Using log-normal distributions forbids ground-state energies, excited state energy differences and amplitudes moving too close to zero or becoming negative, improving stability of the fit.

Priors for ground state energies E_0^M and amplitudes a_0^M are set according to an empirical-Bayes approach, plots of the effective amplitude of the correlation functions are inspected to deduce reasonable priors. The ground-state oscillating parameters $a_0^{M,o}, E_0^{M,o}$, are given the same priors as the non-oscillating states, with uncertainties inflated by 50%. The resulting priors always have a standard deviation at least 10 times that of the final result. The logs of the excited-state energy differences are given prior values $2a\Lambda_{\text{QCD}} \pm a\Lambda_{\text{QCD}}$ where Λ_{QCD} was taken as 0.5 GeV. The log of oscillating and non-oscillating excited state amplitudes are given priors of -1.9 ± 3.3 . The ground-state nonoscillating to nonoscillating three-point parameter, J_{00}^{nn} is given a prior of 1 ± 0.5 , and the rest of the three-point parameters J_{jk}^{nn} are given 0 ± 1 .

The physical quantities that we need here are extracted from the ground-state fit parameters and given in Tables III and IV. E_0^M are the ground-state meson energies in lattice units. For mesons at rest, this corresponds to the mass of the meson, i.e., $E_0^M = aM_M$. The annihilation amplitude for an M -meson at rest is given in lattice units by

TABLE IV. Parameters from our correlation function fits at varying q^2 points. $f_{0,+}^s(q^2)$ are extracted via (22) and (24). The final two columns give the ratio of these form factors to $f_{H_c}\sqrt{M_{H_c}}$. We show statistical/fit errors on each of the quantities, including the value of q^2 that is derived from M_{H_s} and E_{D_s} . q^2 and R^s uncertainties also include those from the determination of the lattice spacing.

| Set | am_h^{val} | $q^2[\text{GeV}^2]$ | aE_{D_s} | $f_0^s(q^2)$ | $f_+^s(q^2)$ | $f_0^s(q^2)/f_{H_c}\sqrt{M_{H_c}}$ | $f_+^s(q^2)/f_{H_c}\sqrt{M_{H_c}}$ |
|------------|---------------------|---------------------|--------------|--------------|--------------|------------------------------------|------------------------------------|
| 1 | 0.5 | 0.01584(17) | 0.90217(11) | 1.0009(14) | | 1.394(11) | |
| | | 0.00026(50) | 0.90386(11) | 0.9997(14) | 0.9997(15) | 1.393(11) | 1.393(11) |
| | 0.65 | 0.2376(26) | 0.90217(11) | 1.0047(28) | | 1.256(11) | |
| | | 0.1201(15) | 0.91308(13) | 0.9956(31) | 1.0014(77) | 1.245(11) | 1.252(14) |
| | 0.8 | 0.0027(12) | 0.92399(15) | 0.9878(31) | 0.9880(32) | 1.235(11) | 1.235(11) |
| | | 0.6874(74) | 0.90217(11) | 1.0092(17) | | 1.1488(94) | |
| 0.3473(40) | | 0.92992(17) | 0.9898(18) | 1.0079(56) | 1.1267(93) | 1.147(11) | |
| 0.0082(29) | | 0.95759(27) | 0.9710(18) | 0.9714(19) | 1.1053(91) | 1.1057(91) | |
| 2 | 0.5 | 0.03014(32) | 0.87715(11) | 1.0004(15) | | 1.369(11) | |
| | | 0.02593(49) | 0.87759(11) | 1.0001(15) | 1.002(19) | 1.369(11) | 1.371(28) |
| | 0.8 | 0.8007(84) | 0.87715(11) | 1.0054(18) | 1.030(18) | 1.1258(91) | 1.154(22) |
| 3 | 0.427 | 0.6126(66) | 0.89178(15) | 0.9948(22) | | 1.1139(91) | |
| | | 0.3715(42) | 0.59151(11) | 0.9942(24) | | 1.250(11) | |
| | 0.525 | 0.1877(26) | 0.60220(14) | 0.9807(26) | 0.9928(61) | 1.233(11) | 1.248(13) |
| | | 0.0053(23) | 0.61281(17) | 0.9685(26) | 0.9688(26) | 1.218(11) | 1.218(11) |
| | 0.65 | 0.954(11) | 0.59151(11) | 0.9876(25) | | 1.152(10) | |
| | | 0.5361(66) | 0.61281(17) | 0.9614(27) | 0.9901(80) | 1.121(10) | 1.155(13) |
| | | 0.0124(54) | 0.63946(31) | 0.9320(31) | 0.9326(31) | 1.0870(99) | 1.0876(99) |
| | | 2.036(23) | 0.59151(11) | 0.9791(28) | | 1.0548(95) | |
| | 0.8 | 0.950(12) | 0.63946(31) | 0.9227(37) | 0.9611(81) | 0.9940(93) | 1.035(12) |
| | | 0.007(13) | 0.68113(58) | 0.8821(42) | 0.8823(41) | 0.9503(92) | 0.9505(92) |
| 3.772(43) | | 0.59151(11) | 0.9709(37) | | 0.9643(90) | | |
| 1.435(22) | | 0.68113(58) | 0.8731(53) | 0.9138(93) | 0.8671(90) | 0.908(12) | |
| 4 | 0.5 | -0.030(44) | 0.7373(17) | 0.825(10) | 0.8242(97) | 0.819(12) | 0.819(12) |
| | | 2.634(32) | 0.439899(86) | 0.9741(28) | | 1.0319(99) | |
| | 0.65 | 1.179(16) | 0.48514(23) | 0.9134(32) | 0.9522(63) | 0.9676(95) | 1.009(11) |
| | | -0.027(18) | 0.52261(54) | 0.8666(45) | 0.8657(44) | 0.9181(96) | 0.9172(96) |
| | 0.8 | 5.497(67) | 0.439899(86) | 0.9575(34) | | 0.9287(91) | |
| | | 3.748(47) | 0.48514(23) | 0.8985(39) | 1.004(18) | 0.8714(88) | 0.974(19) |
| | | 2.301(35) | 0.52261(54) | 0.8529(55) | 0.913(11) | 0.8272(92) | 0.886(13) |
| | | 0.198(93) | 0.5770(24) | 0.770(15) | 0.775(14) | 0.746(16) | 0.751(15) |
| | 0.8 | 9.20(11) | 0.439899(86) | 0.9433(40) | | 0.8508(86) | |
| | | 5.495(72) | 0.52261(54) | 0.8438(67) | 0.974(23) | 0.7611(92) | 0.878(22) |
| | | 3.06(11) | 0.5770(24) | 0.768(16) | 0.842(23) | 0.693(15) | 0.759(22) |
| | | 0.19(26) | 0.6410(57) | 0.721(27) | 0.724(25) | 0.650(25) | 0.653(23) |

$$\langle 0|\tilde{\Phi}_M|M\rangle_{\text{lat}} = \sqrt{2M_M}a_0^M. \quad (20)$$

If $\tilde{\Phi}_M$ is a $\gamma_5 \otimes \gamma_5$ pseudoscalar operator P , the decay constant can be found from this via

$$f_M = \frac{m_{q_0}^{\text{val}} + m_{q'_0}^{\text{val}}}{M_M^2} \langle \Omega|P|M\rangle_{\text{lat}}, \quad (21)$$

where q, q' are the quark flavors that M is charged under. We use this to determine the H_c meson decay constant in Table III. The current matrix elements that we are focused on here can be extracted from the fit parameters via

$$\langle D_s|J|H_s\rangle_{\text{lat}} = 2\sqrt{M_{H_s}E_{D_s}}J_{00}^{nn}. \quad (22)$$

These can be converted into values for the form factors once the currents have been normalized (Sect. II D).

Figure 2 shows the results of a number of tests we performed on the fits to correlators on the fine ensemble. Each test modifies one of the features of the fits and we then plot the resultant value of the key output parameter J_{00}^{nn} . The robustness of the fits can be gauged by the effect of these changes, which are all small.

Figure 3 shows a comparison of the D_s meson dispersion relation on the fine (set 1) and superfine (set 3) lattices. The dispersion relation is sensitive to discretization effects in our quark action. The figure shows them to be small (see [63] for more discussion of discretization effects in dispersion relations for mesons using HISQ quarks). These discretization effects, along with all other discretization effects, are dealt with systematically via the continuum extrapolation detailed in Sec. II E.

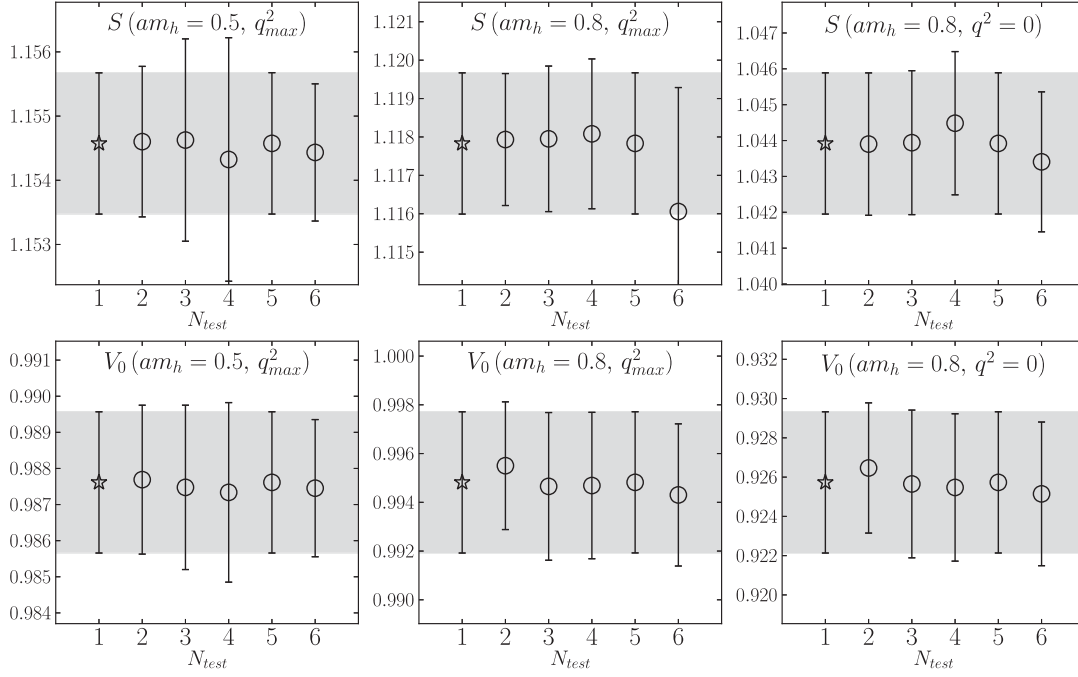


FIG. 2. Tests on the correlator fits on the fine ensemble. The y-axis shows the best fit result for J_{00}^n , with the appropriate current, heavy mass and q^2 specified. At $N_{\text{test}} = 1$ we give our final result, reproduced by the light grey band for ease of comparison. $N_{\text{test}} = 2$ and 3 give the results of setting $N_{\text{exp}} = 4$ and 6 respectively. $N_{\text{test}} = 4$ gives the result of setting $t_{\text{cut}} = 3$ for all 2-point correlators (in the final fit $t_{\text{cut}} = 2$ for all correlators). $N_{\text{test}} = 5$ gives the value when the prior width on the J_{00}^n parameters is doubled. $N_{\text{test}} = 6$ gives the results from the output from a fit to the appropriate correlators from that heavy mass and q^2 value only, and therefore not including correlation with results from other masses and momentum values.

D. Current normalization

In the HISQ formalism, the local scalar current ($1 \otimes 1$) (multiplied by the mass difference of flavors it is charged under) is conserved, and hence requires no renormalization. This is not the case for the local temporal vector current

($\gamma^0 \otimes \gamma^0$). We use this instead of the conserved vector current because it is much simpler, but we then require a renormalization factor to match to the continuum current. This is simple to obtain fully nonperturbatively within this calculation [31,64], at no additional cost.

When both meson states in the matrix elements are at rest (the zero recoil point), the scalar and local vector matrix elements are related via the PCVC relation:

$$(M_{H_s} - M_{D_s})Z_V \langle D_s | V^0 | \hat{H}_s \rangle |_{\text{lat}} = (m_{h0}^{\text{val}} - m_{c0}^{\text{val}}) \langle D_s | S | H_s \rangle |_{\text{lat}}. \tag{23}$$

Z_V can be extracted from this relation using the matrix elements we have computed. The Z_V values found on each ensemble and for each am_{h0}^{val} are given in Table V.

We also remove $\mathcal{O}(am_h^4)$ tree-level mass-dependent discretization effects from the current using a normalization constant, Z_{disc} derived in [65] and discussed in detail in [49]. Z_{disc} values are also tabulated in Table V; they have only a very small effect.

Combining these normalizations with the lattice current from the simultaneous correlation function fits, we find values for the form factors at a given heavy mass, lattice spacing, and q^2 :

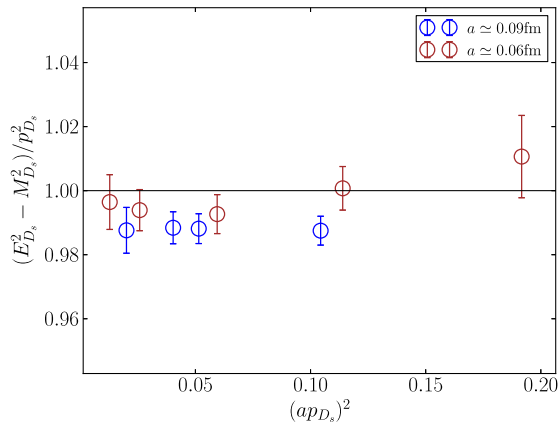


FIG. 3. A comparison of the relativistic dispersion relation for our D_s mesons on gluon field ensemble sets 1 and 3. We plot the square of the “speed of light” against the square of the spatial momentum of the D_s in lattice units. Values on the coarser lattices, set 1, show a small deviation from 1 that is reduced on the finer lattices.

TABLE V. Normalization constants applied to the lattice currents in Eq. (24). Z_V is found from Eq. (23) and Z_{disc} from [49].

| Set | am_{h0}^{val} | Z_V | Z_{disc} |
|-----|------------------------|------------|-------------------|
| 1 | 0.5 | 1.0155(23) | 0.99819 |
| | 0.65 | 1.0254(35) | 0.99635 |
| | 0.8 | 1.0372(32) | 0.99305 |
| 2 | 0.5 | 1.0134(24) | 0.99829 |
| | 0.8 | 1.0348(29) | 0.99315 |
| 3 | 0.427 | 1.0025(31) | 0.99931 |
| | 0.525 | 1.0059(33) | 0.99859 |
| | 0.65 | 1.0116(37) | 0.99697 |
| | 0.8 | 1.0204(46) | 0.99367 |
| 4 | 0.5 | 1.0029(38) | 0.99889 |
| | 0.65 | 1.0081(43) | 0.99704 |
| | 0.8 | 1.0150(49) | 0.99375 |

$$\begin{aligned}
 f_0^s(q^2) &= \frac{m_{h0}^{\text{val}} - m_{c0}^{\text{val}}}{M_{H_s}^2 - M_{D_s}^2} Z_{\text{disc}} \langle D_s | S | H_s \rangle_{\text{lat}}(q^2) \\
 f_+^s(q^2) &= \frac{Z_{\text{disc}}}{2M_{H_s}} \\
 &\quad \times \frac{\delta^M \langle D_s | S | B_s \rangle_{\text{lat}}(q^2) - q^2 Z_V \langle D_s | V^0 | B_s \rangle_{\text{lat}}(q^2)}{\mathbf{p}_{D_s}^2},
 \end{aligned} \tag{24}$$

where δ^M is defined in Eq. (6) and we have made the dependence of the matrix elements on q^2 explicit.

E. Obtaining a result at the physical point

We now discuss how we fit our results for $f_0^s(q^2)$ and $f_+^s(q^2)$ as a function of valence heavy quark mass, sea light quark mass and lattice spacing. Evaluating these fits at the mass of the b , with physical l , s and c masses and zero lattice spacing will then give us the physical form factor curves from which to determine the differential decay rate, using Eq. (2).

Following [49] we use two methods; one a direct approach to fitting the form factors and the other in which we fit the ratio

$$R_{0,+}^s(q^2) \equiv \frac{f_{0,+}^s(q^2)}{f_{H_c} \sqrt{M_{H_c}}}, \tag{25}$$

in which discretization effects are somewhat reduced. We will take our final result from the direct approach and we describe that here. We use the ratio approach as a test of uncertainties and we describe that in more detail in Appendix B.

We use identical fit functions for both approaches. We feed into the fit our results from Tables III and IV, retaining the correlations (not shown in the Tables) between values

for different heavy quark masses and q^2 values on a given gluon field ensemble that we are able to capture in our simultaneous fits (Sec. II C). We also include, where needed, correlated lattice spacing uncertainties.

1. Kinematic behavior

Our fit form is a modified version of the Bourrely-Caprini-Lellouch (BCL) parametrization for pseudoscalar-to-pseudoscalar form factors [66]:

$$\begin{aligned}
 f_0^s(q^2)|_{\text{fit}} &= \frac{1}{1 - \frac{q^2}{M_{H_{c0}}^2}} \sum_{n=0}^{N-1} a_n^0 z^n(q^2), \\
 f_+^s(q^2)|_{\text{fit}} &= \frac{1}{1 - \frac{q^2}{M_{H_c^*}^2}} \\
 &\quad \times \sum_{n=0}^{N-1} a_n^+ \left(z^n(q^2) - \frac{n}{N} (-1)^{n-N} z^N(q^2) \right).
 \end{aligned} \tag{26}$$

The function $z(q^2)$ maps q^2 to a small region inside the unit circle on the complex q^2 plane, defined by

$$z(q^2) = \frac{\sqrt{t_+ - q^2} - \sqrt{t_+ - t_0}}{\sqrt{t_+ - q^2} + \sqrt{t_+ - t_0}}. \tag{27}$$

Here $t_+ = (M_{H_s} + M_{D_s})^2$ and we choose t_0 to be $t_0 = 0$. This t_0 choice means that $q^2 = 0$ maps to $z = 0$ and the fit functions simplify to $f_{0,+}^s(0) = a_{0,+}^s$. For the physical range of q^2 for B_s to D_s decay, the range covered by z is $|z| < 0.06$, resulting in a rapidly converging series in powers of z . We truncate at $N = 3$; adding further powers of z^n does not effect the results of the fit.

The factors in front of the sums in the BCL parametrization account for lowest mass pole expected in the full q^2 plane for each form factor coming from the production of on-shell H_{c0} and H_c^* states in the crossed channel of the semileptonic decay. Note that these poles, even though they are below the cut (for $H_s + D_s$ production) that begins at t_+ , are at much higher q^2 values than those covered by the semileptonic decay here (with maximum q^2 given by $(M_{H_s} - M_{D_s})^2$).

We must estimate $M_{H_{c0}}$, the scalar heavy-charm meson mass, at each of the heavy masses we use. For this we use the fact that the splitting $\Delta_0 = M_{H_{c0}} - M_{H_c}$ is an orbital excitation and therefore largely independent of the heavy quark mass. The splitting has been calculated in [67] to be $\Delta_0 = 0.429(13)$ GeV at the b quark mass. Combined with an H_c mass from our lattice results, we construct the H_{c0} mass as $M_{H_{c0}} = M_{H_c} + \Delta_0$. We do not include the uncertainty on Δ_0 in the fit, since any shift in the precise position of the pole will be absorbed into the other fit parameters.

To estimate $M_{H_c^*}$, the vector heavy-charm meson mass, we use the fact that the hyperfine splitting $M_{H_c^*} - M_{H_c}$ should vanish in the infinite m_h limit. $M_{H_c^*}$ then takes the

approximate form $M_{H_c^*} \simeq M_{H_c} + \mathcal{O}(1/m_h)$. To reproduce this behavior we use the ansatz $M_{H_c^*} = M_{H_c} + x/M_{\eta_h}$, and fix x at the b quark mass using the value of $M_{H_c^*} - M_{H_c}$ from [67]. This gives $x = 0.507 \text{ GeV}^2$.

2. Heavy quark mass and discretization effects

To account for dependence on the heavy quark mass and discretization effects in a general way, we use the following form for each of the $a_n^{0,+}$ coefficients:

$$a_n^{0,+} = \left(1 + \rho_n^{0,+} \log \left(\frac{M_{\eta_h}}{M_{\eta_c}} \right) \right) \times \sum_{i,j,k=0}^{2,2,2} d_{ijkn}^{0,+} \left(\frac{2\Lambda_{\text{QCD}}}{M_{\eta_h}} \right)^i \left(\frac{am_{h0}^{\text{val}}}{\pi} \right)^{2j} \left(\frac{am_{c0}^{\text{val}}}{\pi} \right)^{2k} \times (1 + \mathcal{N}_{\text{mistuning},n}^{0,+}). \quad (28)$$

To understand this form, focus first on the terms inside the sum. Powers of $(2\Lambda_{\text{QCD}}/M_{\eta_h})$ allow for variation of the coefficients as the heavy quark mass changes, using an HQET-inspired form since this is a heavy-light to heavy-light meson transition. $M_{\eta_h}/2$ is proportional to m_h at leading order in HQET, so is a suitable physical proxy for the heavy quark mass. We take Λ_{QCD} here to be 0.5 GeV. The other two terms in the sum allow for discretization effects. These can be set by two scales. One is the variable heavy quark mass am_{h0}^{val} and the other is the charm quark mass, am_{c0}^{val} , constant on a given ensemble. Adding further discretization effects set by smaller scales such as $a\Lambda_{\text{QCD}}$ had no impact on the results since such effects are subsumed into the larger am_{c0}^{val} terms.

The coefficients $d_{ijkn}^{0,+}$ are fit parameters given Gaussian prior distributions of 0 ± 2 .

To account for any possible logarithmic dependence on m_h , arising from, for example, an ultraviolet matching between HQET and QCD, we include a log term in front of the sum. $\rho_n^{0,+}$ are fit parameters with prior distribution 0 ± 1 .

The fact that $f_+^s(0) = f_+^c(0) (\Rightarrow a_0^+ = a_0^0)$ is a powerful constraint within the heavy-HISQ approach. Since this relation must be true at all m_h , it translates to constraints on the fit parameters; $d_{i000}^+ = d_{i000}^0 \forall i$ and $\rho_0^+ = \rho_0^0$. We impose these constraints in the fit.

3. Quark mass mistuning

To account for any possible mistunings in the c , s and l quark masses, we include the terms $\mathcal{N}_{\text{mistuning},n}^{0,+}$ in each $a_n^{0,+}$ coefficient, defined by

$$\mathcal{N}_{\text{mistuning},n}^{0,+} = \frac{c_{s,n}^{\text{val},0,+} \delta_s^{\text{val}} + c_{s,n}^{0,+} \delta_s + 2c_{l,n}^{0,+} \delta_l}{10m_s^{\text{tuned}}} + c_{c,n}^{0,+} \left(\frac{M_{\eta_c} - M_{\eta_c}^{\text{phys}}}{M_{\eta_c}^{\text{phys}}} \right). \quad (29)$$

Here $c_{l,n}^{0,+}$, $c_{s,n}^{0,+}$ and $c_{s,n}^{(\text{val}),0,+}$ are fit parameters with prior distributions 0 ± 1 .

We define $\delta_s^{(\text{val})} = m_{s0}^{(\text{val})} - m_s^{\text{tuned}}$ [54], where m_s^{tuned} is given by

$$m_s^{\text{tuned}} = m_{s0} \left(\frac{M_{\eta_s}^{\text{phys}}}{M_{\eta_s}} \right)^2. \quad (30)$$

M_{η_s} is the mass of an unphysical pseudoscalar $s\bar{s}$ meson where the valence quarks are artificially not allowed to annihilate; its mass (in the continuum and chiral limits) can be determined in lattice QCD calculations in terms of the masses of the π and K mesons. In [54] this analysis was done to yield $M_{\eta_s} = 0.6885(20) \text{ GeV}$. This is the value that we use here for $M_{\eta_s}^{\text{phys}}$ to tune the s quark mass. $M_{\eta_c}^{\text{phys}}$ is taken to be 2.986(3) GeV from [54]. This allows for a small (0.1%) adjustment for $c\bar{c}$ annihilation and QED effects, neither of which are included in our calculation.

We similarly account for (sea) light quark mass mistuning by defining $\delta_l = m_{l0} - m_l^{\text{tuned}}$. We find m_l^{tuned} from m_s^{tuned} , using the fact that the ratio of quark masses is regularization independent, and was determined in [45]:

$$\left. \frac{m_s}{m_l} \right|_{\text{phys}} = 27.18(10). \quad (31)$$

We set m_l^{tuned} to m_s^{tuned} divided by this ratio.

All higher order contributions, such as $\delta_{s,l}^2$, $(M_{\eta_c} - M_{\eta_c}^{\text{phys}})^2$, or $(\Lambda_{\text{QCD}}/M_{\eta_h})^2$ are too small to be resolved by our lattice data, so are not included in the fit.

In our lattice QCD calculation we set $m_u = m_d \equiv m_l$; this means that our results do not allow for strong-isospin breaking in the sea quarks. By moving the m_l^{tuned} value up and down by the PDG value for $m_d - m_u$ [28], we found that any impact of strong-isospin breaking on our results was negligible.

4. Finite-volume and topology freezing effects

We expect finite-volume effects to be negligible in our calculation and we do not include any associated error. Finite-volume corrections to the $B \rightarrow D \ell \nu$ form factors were calculated in chiral perturbation theory in [33] and found to be very small, less than one part in 10^4 , for typical lattice QCD calculations. For $B_s \rightarrow D_s \ell \nu$ form factors we expect finite-volume effects to be smaller than this because there are no valence u/d quarks.

The finest lattices that we use here have been shown to have only a slow variation of topological charge in Monte Carlo time. This means that averaging results over the ensemble could introduce a bias if the quantities we are studying are sensitive to topological charge. A study calculating the adjustment needed to allow for this gives only a 0.002% effect on the D_s decay constant [68]. For B_s

to D_s form factors we might expect an effect of similar relative size. This is negligible compared to our other uncertainties.

5. Uncertainties in the physical point

Once we have fit our lattice results as described above, we can determine the physical form factors by setting $a = 0$, $M_{\eta_h} = M_{\eta_b}$. We also take $M_{H_c} = M_{B_c}$, $M_{\eta_c} = M_{\eta_c}^{\text{phys}}$, $m_{l0} = m_l^{\text{tuned}}$, and $m_{s0} = m_s^{\text{tuned}}$. We take the experimental value for M_{η_b} but allow for an additional ± 10 MeV uncertainty beyond the experimental uncertainty, since our lattice QCD results do not allow for QED effects or for η_b annihilation to gluons [44]. This additional uncertainty has no effect, however, because the heavy quark mass dependence is mild.

III. RESULTS AND DISCUSSION

In Tables III and IV, we give our results for the form factors on each ensemble along with the meson masses needed for the fits of the form factors as a function of m_h and a discussed in Sec. II E.

We first show results from simplified fits to zero recoil data to find $f_{0,+}^s(q_{\text{max}}^2)$. This allows us to test the behavior in m_h . We then perform the larger fit, described in Sec. II E, taking into account all the lattice data throughout the q^2 range.

A. Zero recoil

We performed a fit to $f_0^s(q_{\text{max}}^2)$ as a function of m_h and a using the fit form

$$f_0^s(q_{\text{max}}^2)|_{\text{fit}} = \left(1 + \rho \log\left(\frac{M_{\eta_h}}{M_{\eta_c}}\right)\right) \times \sum_{i,j,k=0}^{2,2,2} d_{ijk} \left(\frac{2\Lambda_{\text{QCD}}}{M_{\eta_h}}\right)^i \left(\frac{am_{h0}^{\text{val}}}{\pi}\right)^{2j} \left(\frac{am_{c0}^{\text{val}}}{\pi}\right)^{2k} \times (1 + \mathcal{N}_{\text{mistuning}}). \quad (32)$$

This is the same fit function as described earlier for the individual z -space coefficients in Eq. (28) and we take the same priors for the corresponding coefficients as discussed there.

The fit has $\chi^2/N_{\text{dof}} = 0.21$, for 12 degrees of freedom. Evaluating the result at $a = 0$ and physical b quark mass, we find

$$f_0^s(q_{\text{max}}^2) = 0.907(16). \quad (33)$$

We show the dependence on M_{η_h} of our results and the fit in Fig. 4. The error budget corresponding to Eq. (33) is given in Table VI. Note that we do not impose the constraint that $f_0^s(q_{\text{max}}^2) = 1.0$ when $m_h = m_c$. If we do this, we reduce the uncertainty in Eq. (33) by 25%.

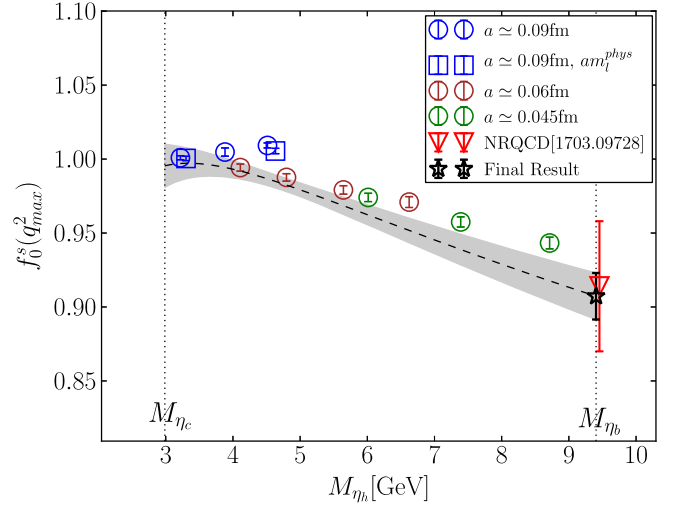


FIG. 4. $f_0^s(q_{\text{max}}^2)$ against M_{η_h} (a proxy for the heavy quark mass). The circle, square and triangular points show lattice results, i.e., outputs from the correlator fits. The grey band shows the result of our fit at $a = 0$ and physical l , s and c masses. Notice that the y -axis scale does not begin at zero. We also include the result from a previous lattice calculation, which used the NRQCD discretization for the b quark with a nonrelativistic expansion of the current through $\mathcal{O}(\Lambda/m_b)$ and $\mathcal{O}(\alpha_s)$ matching to continuum QCD [35]. Sets of gluon field configurations listed in the legend follow the order of sets in Table I.

We include in Fig. 4 a previous lattice determination of $f_0^s(q_{\text{max}}^2)$ [35], shown as a red triangle. Our result, containing independent uncertainties, is in agreement with this earlier value but much more accurate. The older study used the $n_f = 2 + 1$ MILC asqtad gluon ensembles, with HISQ s and c valence quarks, and an NRQCD b quark. Using NRQCD meant that the calculation could be performed directly at the physical b mass. However, the matching of lattice NRQCD currents to continuum QCD, performed at $\mathcal{O}(\alpha_s)$, is a significant source of systematic error absent in our calculation.

We perform a number of tests of the fit at zero recoil, and present results in Fig. 5. The tests show that the fits are robust.

B. Full q^2 range

We now proceed to fit our full set of data including zero and nonzero recoil points to the fit form given in Eqs. (26) and (28) and discussed in Sec. II E. We include the

TABLE VI. Error budget for $f_0^s(q_{\text{max}}^2)$.

| Source | % Fractional error |
|---|--------------------|
| Statistics | 1.11 |
| $m_h \rightarrow m_b$ and $a \rightarrow 0$ | 1.20 |
| Quark mistuning | 0.58 |
| Total | 1.73 |

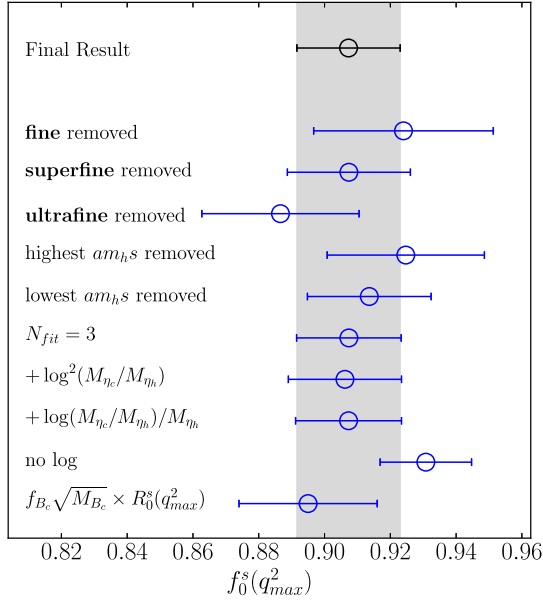


FIG. 5. Results of tests of the $f_0^s(q_{\max}^2)$ fit. The top three blue points show $f_0^s(q_{\max}^2)$ at continuum and physical b mass, if data from the fine, superfine or ultrafine ensembles are not used in the fit. The fourth and fifth blue points show the result if data at the highest/lowest am_h value on each ensemble are removed. The point labeled $N_{\text{fit}} = 3$ is the result of extending the sum in Eq. (28) so that it truncates at 3 rather than 2 in each of the i, j, k directions. The points labeled $+\log^2(M_{\eta_c}/M_{\eta_h})$ represents the result of adding a $\rho_2 \log^2(M_{\eta_h}/M_{\eta_c})$ term in the first set of brackets in Eq. (28), where ρ_2 is a new fit parameter with the same prior distribution as ρ . Similarly for the $+\log(M_{\eta_h}/M_{\eta_c})/M_{\eta_h}$ point. The point labelled “no log” results from omitting the factor $(1 + \rho \log(M_{\eta_c}/M_{\eta_h}))$. The lowest point shows the value from the fit result for $R_0^s(q_{\max}^2)$, multiplied by the experimental value for $\sqrt{M_{B_c}}$ [28] and the result of our determination of f_{B_c} at the physical point detailed in Appendix A of [49].

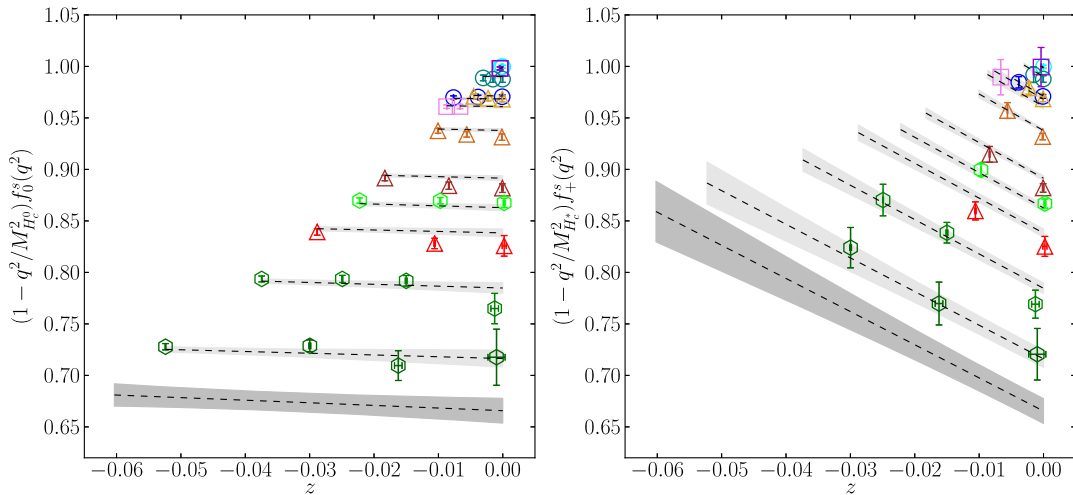


FIG. 6. $P f_{0,+}^s$ in z -space, where P is the appropriate pole function for each form factor given in Eq. (26). The colored points show lattice results, i.e., outputs from the correlator fits. The colors correspond to the legend given in Fig. 7. Sets listed in this legend follow the order of sets in Table I. The lowest grey band shows the result of our fit at $a = 0$ and physical l, s, c and b masses. Each of the higher grey bands show the fit form evaluated at the heavy quark masses, lattice spacings and l, s and c masses of each of our sets of lattice data.

covariance matrix between the form factor values obtained from correlator fits on a given ensemble along with correlated lattice spacing uncertainties. The goodness of fit obtained is $\chi^2/N_{\text{dof}} = 0.51$, with 58 degrees of freedom. The fit parameters that are constrained by the fit are listed in Table X of Appendix C.

In Fig. 6 we show our results and fit function in z -space for the product $P \times f$ of each form factor and its pole factor, P , given by $1 - q^2/M_{H_c}^{0,*}$ in Eq. (26). This shows that the z -dependence of $P \times f$ is relatively benign for both form factors and the main m_h -dependent effect is the smooth reduction in value of $P \times f$ as m_h increases. The final result at the physical b quark mass is given by the grey band.

In Fig. 7, we show the results and fit function in q^2 -space. The form factors for the physical b quark mass (i.e., those corresponding to $B_S \rightarrow D_S$ decay) are given by the grey band.

From Fig. 6 it is clear that the largest effect in the lattice results is a z -independent shift as a function of heavy quark mass. Not surprisingly then, the parameters that are best constrained by the fit are $d_{i000}^0 = d_{i000}^+$ and $\rho_0^0 = \rho_0^+$, i.e., the parameters that control this heavy-quark mass extrapolation. We find that $d_{1000}^{0,+} = 1.397(82)$ and $\rho_0^{0,+} = 0.419(20)$. Other coefficients are not as well constrained by the fit, including those that allow for discretization effects. Allowing for such terms in the fit, however, means that their impact on the final uncertainty is included.

Figure 8 shows the physical f_+ and f_0 form factors on the same plot and covering the full q^2 range for the $B_S \rightarrow D_S$ decay. Figure 9 plots the associated error budget for the two form factors throughout the q^2 range. The dominant uncertainty comes from statistical errors. There are also significant uncertainties from the q^2 and m_h dependence for

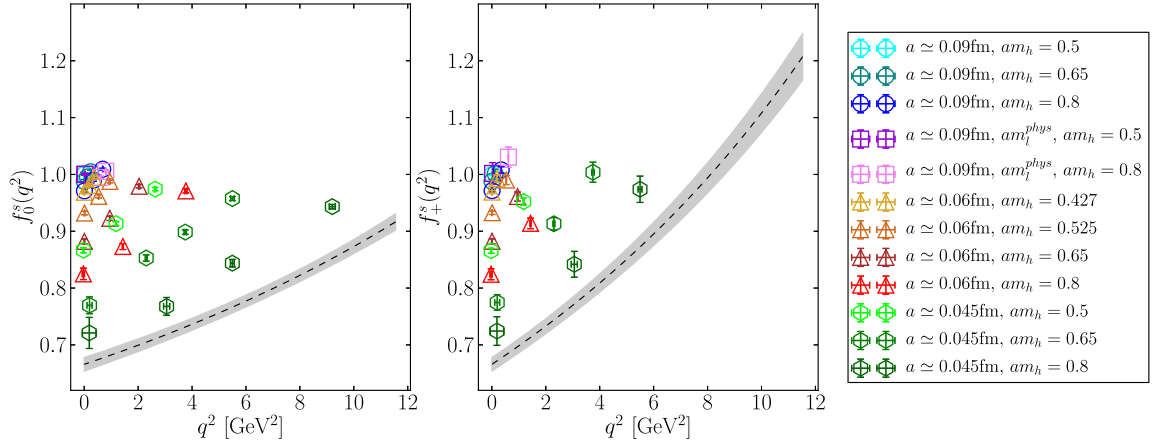


FIG. 7. $f_{0,+}^s(q^2)$ plotted against q^2 . The colored points show lattice results, i.e., outputs from the correlator fits. The grey band shows the result of our fit at $a = 0$ and physical l, s, c and b masses. Sets listed in the legend follow the order of sets in Table I.

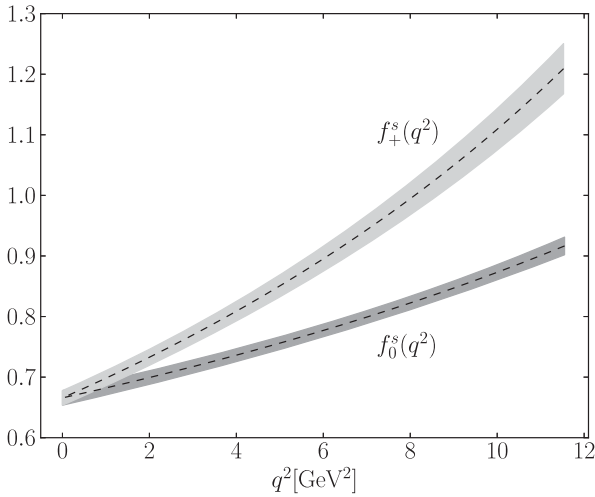


FIG. 8. Final result for $f_{0,+}^s(q^2)$ against q^2 at the physical point.

f_+ at larger values of q^2 . This is because there are no lattice QCD results at q_{\max}^2 for f_+ . The impact of uncertainties in the lattice spacing (both in w_0/a and in w_0) are smaller than the errors shown in the figure and so not plotted there. This is because the form factors themselves are dimensionless and lattice spacing effects in the determination of q^2 largely cancel as, for example, the pole masses are given in terms of lattice masses.

As discussed in Sec. II E an alternative approach to the fit is to take ratios of the form factors to the H_c decay constant and fit the ratios to the fit form of Eqs. (26) and (28). This fit is described in Appendix B. It has the advantage of smaller discretization effects but the disadvantage of larger lattice spacing uncertainties because the ratios being fit are dimensional. In the end the ratio method has larger uncertainty for the final physical form factors. We therefore take the results from the direct method as our final result, and use the ratio method results as a consistency test. Since the two approaches have quite different systematic errors,

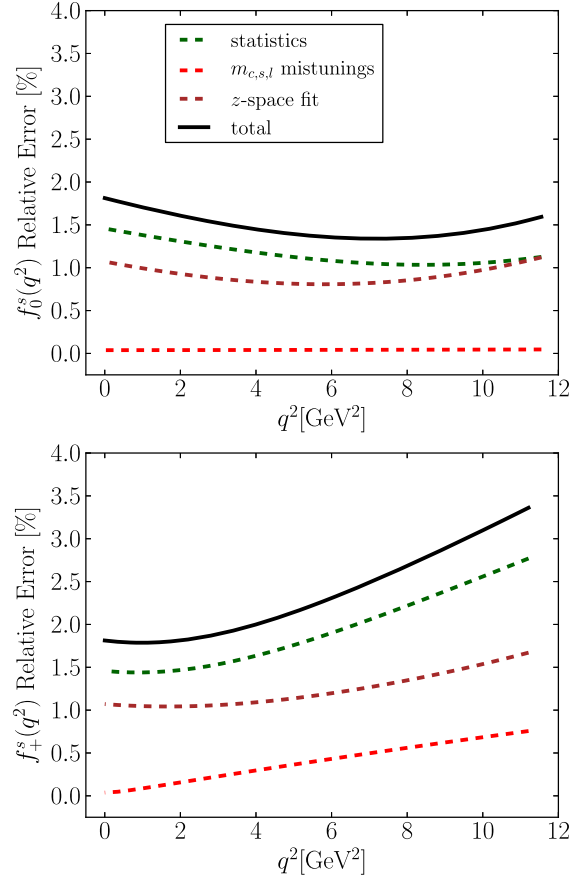


FIG. 9. Error budget for $f_{0,+}^s(q^2)$ as a function of q^2 .

their comparison supplies a strong consistency check. In Fig. 10, we plot the form factors from the two methods on top of each other. As is clear from this plot, the results are in good agreement. The direct method gives a more accurate result for both form factors and at all q^2 .

We compare the coefficients from our fits to unitarity bounds in Appendix D as a further test.

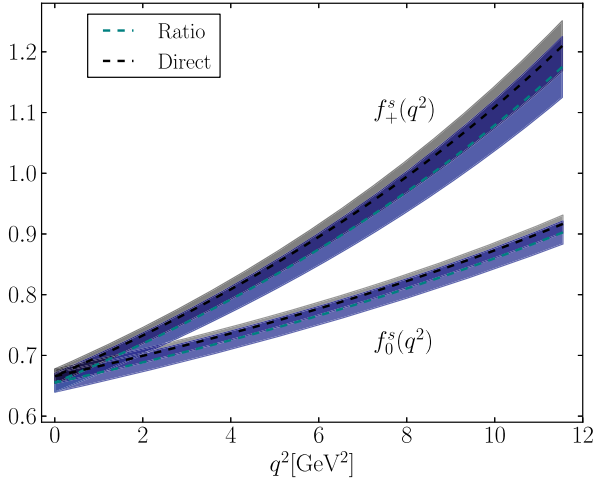


FIG. 10. Results for $f_{0,+}^s(q^2)$ against q^2 at the physical point, comparing the ratio method (from Appendix B) and the direct method (from Sec. III B).

In Fig. 11, we compare our final form factors to those determined from the lattice QCD calculation using the NRQCD approach for the b quark already used as a comparison at q_{max}^2 in Fig. 4 [35]. The NRQCD calculation works directly at the b quark mass but on relatively coarse lattices and hence is unable to obtain results at large physical momenta for the D_s meson. The results close to zero-recoil are extrapolated to $q^2 = 0$ using a z -space parametrization. As the figure shows, our results are in excellent agreement with the NRQCD calculation but are more precise for both $f_0^s(q^2)$ and $f_+^s(q^2)$ throughout all q^2 . This is because we can avoid the significant systematic

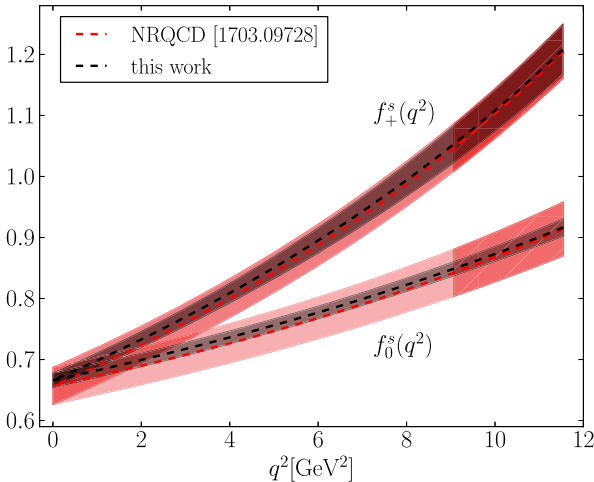


FIG. 11. Our final result for $f_{0,+}^s(q^2)$ compared to form factors calculated using an NRQCD action for the b quark [35]. Part of the NRQCD band is shaded darker than the rest ($q^2 \gtrsim 9.5 \text{ GeV}^2$) to signify the region where lattice results were directly calculated. The NRQCD form factors in the rest of the q^2 range are the result of an extrapolation using a BCL parametrization.

uncertainty that the NRQCD calculation has from the perturbative matching to continuum QCD of the NRQCD current that couples to the W .

The $B_s \rightarrow D_s \ell \nu$ form factors have also recently been obtained by the Fermilab Lattice/MILC collaborations from their earlier $B \rightarrow D$ form factors and ratios of $B_s \rightarrow D_s$ and $B \rightarrow D$ form factors using the Fermilab formalism for b and c quarks in [69]. Our results are consistent with theirs (shown in Fig. 20 of [69]) but we have a smaller uncertainty at $q^2 = 0$.

C. $R(D_s)$

Using our calculated form factors $f_{0,+}^s(q^2)$, we can calculate the differential rate for $B_s \rightarrow D_s \ell \nu$ decay from Equation (1). This is a function of the lepton mass and so differs between the heavy τ and the light e, μ leptons. The differential rate for μ and τ is compared in Fig. 12. We take the meson and lepton masses needed for Eq. (1) from [28] and $\eta_{\text{EW}} = 1.011(5)$ [23]. The distribution in the τ case is cut off at $q^2 = m_\tau^2$ and so, although there is enhancement from m_ℓ^2/q^2 terms in Eq. (1) that reflect reduced helicity suppression, the integrated branching fraction for the τ case is smaller than for the μ .

The ratio of branching fractions for semileptonic B decays to τ and to e/μ is being used as a probe of lepton universality with an interesting picture emerging [36,37]. Here we provide a new SM prediction for the quantity

$$R(D_s) = \frac{\mathcal{B}(B_s \rightarrow D_s \tau \nu_\tau)}{\mathcal{B}(B_s \rightarrow D_s l \nu_l)}, \quad (34)$$

where $l = e$ or μ [the difference between e and μ is negligible in comparison to our precision on $R(D_s)$]. Our result is

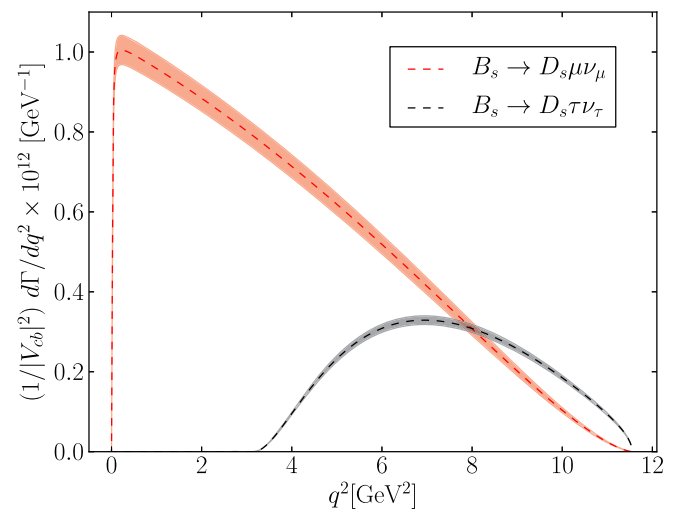


FIG. 12. Differential decay rates for the $B_s \rightarrow D_s \mu \nu_\mu$ and $B_s \rightarrow D_s \tau \nu_\tau$ decays, calculated using the form factors determined in this work.

TABLE VII. Error budget for our result for $R(D_s)$ in the SM. z -space fit refers to the error associated with the fit of the dependence on heavy quark mass and lattice spacing and interpolation in q^2 .

| Source | % Fractional error |
|----------------------|--------------------|
| Statistics | 1.11 |
| z -space fit | 1.05 |
| Quark mass mistuning | 0.12 |
| Total | 1.54 |

$$R(D_s)|_{\text{SM}} = 0.2993(46), \quad (35)$$

in which we averaged over the $l = e$ and $l = \mu$ cases. Note that $|V_{cb}|$ and η_{EW} cancel in this ratio. We give an error budget for this result in terms of the uncertainties from our lattice QCD calculation in Table VII. Our result agrees with, but is more accurate than, the previous lattice QCD value of $R(D_s)$ [0.301(6)] from [35]. An experimental result for $R(D_s)$ would allow a new test of lepton universality.

We expect very little difference between $R(D_s)$ and the analogous quantity $R(D)$ because the mass of the spectator quark has little effect on the form factors [34]. Lattice QCD calculations that involve light spectator quarks have larger statistical errors, however, which is why the process $B_s \rightarrow D_s$ is under better control. Previous lattice QCD results for $R(D)$ are 0.300(8) [23] and 0.299(11) [22], in which any difference with our result for $R(D_s)$ is too small to be visible with these uncertainties.

IV. COMPARISON TO HQET

In Fig. 13 we show our form factor results at two key values of q^2 , the zero recoil point and $q^2 = 0$, as a function of heavy quark mass, given by M_{η_h} . The plot demonstrates

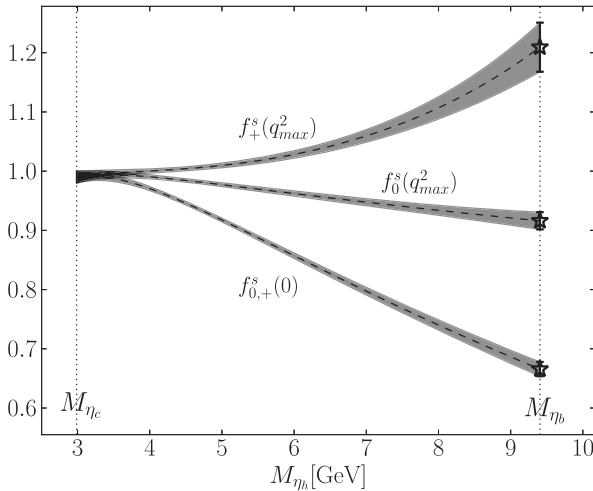


FIG. 13. Form factor values at q_{max}^2 and $q^2 = 0$ plotted against M_{η_h} , a proxy for the heavy quark mass.

how f_+ at zero-recoil increases as the heavy quark mass increases, but f_0 changes very little. The value at $q^2 = 0$, where the form factors are equal, falls with growing heavy quark mass, as the q^2 range opens up.

Knowledge of the functional form of $f_0^s(q^2)$ and $f_+^s(q^2)$, along with $h_{A_1}^s(1)$ from [49], against m_h gives us access to the functional form in m_h of a number of quantities of interest in HQET.

In HQET the vector current matrix element is parametrized with a different set of form factors, $h_+^s(w)$ and $h_-^s(w)$ according to

$$\frac{\langle D_s | V^\mu | H_s \rangle}{\sqrt{M_{D_s} M_{H_s}}} = h_+^s(w)(v + v')^\mu + h_-^s(w)(v - v')^\mu, \quad (36)$$

where $v^\mu = p_{H_s}^\mu/M_{H_s}$ and $v'^\mu = p_{D_s}^\mu/M_{D_s}$ are the 4-velocities of the initial and final state mesons, and $w = v \cdot v'$ is an alternative parameter to q^2 used in the context of HQET.

As a test of HQET, one can construct ratios of form factors that should become unity in the $m_c, m_h \rightarrow \infty$ limit. Following the notation defined in [70], one can redefine the form factors such that each of them reduce to the Isgur-Wise function $\xi(w)$ in the $m_c, m_h \rightarrow \infty$ limit. In the $B_s \rightarrow D_s$ case these new form factors are

$$S_1^s(w) = h_+^s(w) - \frac{1 + r w - 1}{1 - r w + 1} h_-^s(w), \quad (37)$$

$$V_1^s(w) = h_+^s(w) - \frac{1 - r}{1 + r} h_-^s(w), \quad (38)$$

where $r = M_{D_s}/M_{H_s}$. $h_{A_1}^s$ also reduces to ξ in the infinite mass limit. Hence any ratio between S_1^s, V_1^s and $h_{A_1}^s$ should

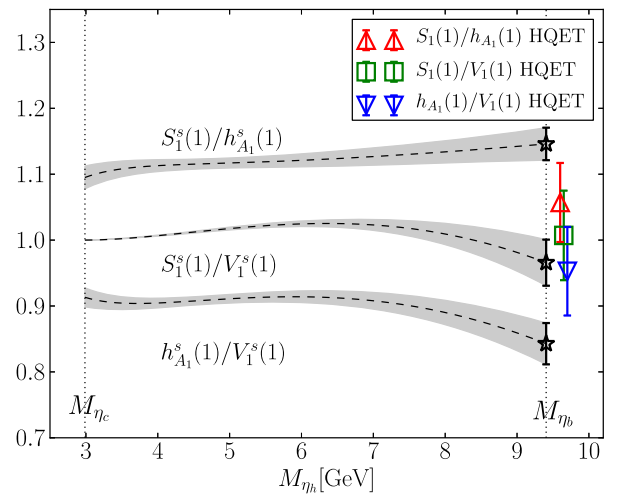


FIG. 14. Form factor ratios against M_{η_h} , a proxy for the heavy quark mass. S_1^s and V_1^s are defined in Eqs. (37) and (38). The colorful points are NLO HQET expectations from [25], derived with input from QCD sum rules.

become unity in this limit. From our results at zero recoil and for $m_h = m_b$ we find

$$\left. \frac{S_1^s(1)}{h_{A_1}^s(1)} \right|_{\text{lat}} = 1.146(25) \quad (39)$$

$$\left. \frac{V_1^s(1)}{V_1^s(1)} \right|_{\text{lat}} = 0.966(35) \quad (40)$$

$$\left. \frac{h_{A_1}^s(1)}{V_1^s(1)} \right|_{\text{lat}} = 0.843(31). \quad (41)$$

Figure 14 illustrates how these ratios vary with m_h , and gives the NLO HQET expectation for these values for comparison [25]. As can be seen here, our results show large deviations from the HQET expectation, implying that NLO HQET is missing significant higher order contributions. As discussed in [71], previous lattice results have shown similarly large deviations. These are also shown in preliminary results from the JLQCD collaboration [72].

Another set of quantities of interest in HQET are the slopes of the form factors at $q^2 = 0$ [73,74]:

$$\frac{1}{\beta(m_h)} \equiv \frac{M_{H_s}^2 - M_{D_s}^2}{f_+^s(0)} \left. \frac{df_+^s}{dq^2} \right|_{q^2=0}, \quad (42)$$

$$\delta(m_h) \equiv 1 - \frac{M_{H_s}^2 - M_{D_s}^2}{f_+^s(0)} \left(\left. \frac{df_+^s}{dq^2} \right|_{q^2=0} - \left. \frac{df_0^s}{dq^2} \right|_{q^2=0} \right). \quad (43)$$

To obtain these values from our results for the form factors, we take the derivative of the fit function [Eq. (28)] evaluated at continuum and physical l , s and c masses. At $m_h = m_b$ we find

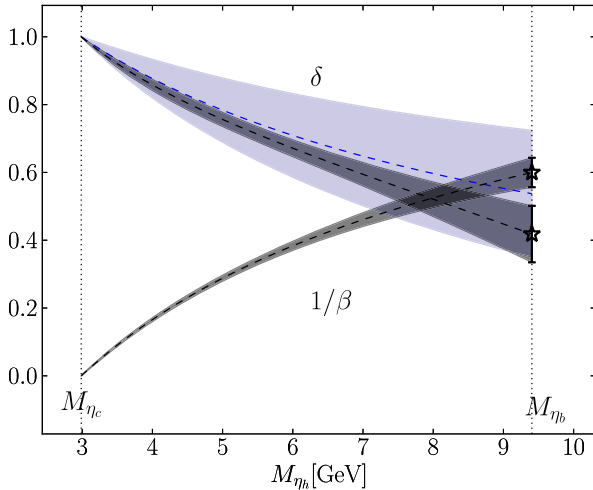


FIG. 15. We show two quantities derived from the form factor slopes as a function of M_{η_h} . $1/\beta(m_h)$ is defined in Eq. (42) and δ in Eq. (43). Our results are shown by the grey bands. The blue band shows the leading order HQET expectation for δ given in Eq. (45).

$$\frac{1}{\beta(m_b)} = 0.600(43), \quad \delta(m_b) = 0.405(84). \quad (44)$$

In Fig. 15 we show how these quantities vary with m_h . By rewriting Eq. (43) in terms of $h_{+,-}^s$, and recognising that in the heavy quark limit $h_+^s \approx \xi$ and $h_-^s \approx 0$, one can find a leading order HQET expectation for δ [74]:

$$\begin{aligned} \delta(m_h) &= \frac{2M_{D_s}}{M_{H_s} + M_{D_s}} \frac{1 + \frac{h_-}{h_+}}{1 - \frac{M_{H_s} - M_{D_s}}{M_{H_s} + M_{D_s}} \frac{h_-}{h_+}} \\ &= \frac{2M_{D_s}}{M_{H_s} + M_{D_s}} [1 + \mathcal{O}(\alpha_s, \Lambda_{\text{QCD}}/m_h, \Lambda_{\text{QCD}}/m_c)]. \end{aligned} \quad (45)$$

This leading order expression is shown in Fig. 15 as a blue band. Our results (grey band) are in good agreement with this, up to the uncertainties from higher order terms shown in Eq. (45).

V. CONCLUSIONS

We have calculated the scalar and vector form factors for the $B_S \rightarrow D_S \ell \nu$ decay for the full q^2 range using lattice QCD with a fully nonperturbative normalization of the current operators for the first time. Our calculation used correlation functions at three values of the lattice spacing, including an ensemble with an approximately physical light quark mass. We used the relativistic HISQ action with a range of values for the heavy valence quark and by fitting this dependence, along with the lattice spacing dependence, we are able to determine results at the b quark mass. The valence c and s quark masses are accurately tuned to their physical values. By working on very fine lattices we are able both to reach a heavy quark mass close to the b but also to cover the full q^2 range of the decay.

Our results for the form factors are given in Fig. 8 and the differential rate that this implies for $B_S \rightarrow D_S \ell \nu$ in Fig. 12. This will allow a determination of $|V_{cb}|$ from future experimental data from this semileptonic process. Instructions on how to reproduce our form factors are given in Appendix A. Our error budget is given in Fig. 9.

Our results are more accurate than previous lattice QCD determinations using a nonrelativistic b quark formalism because we do not have a systematic uncertainty from the perturbative matching of the lattice current to continuum QCD.

From our results we can predict the ratio $R(D_S)$ of the branching fraction to a τ lepton compared to that to e/μ (see Sec. III C). We are also able to compare functions of the form factors and their slopes to HQET expectations (see Sec. IV).

Our calculation shows that a heavy-HISQ determination of the $B \rightarrow D \ell \nu$ form factors is feasible. This would allow direct comparison to existing experimental data. Such a

calculation could use an identical strategy to the one demonstrated here, with the strange valence quark replaced with a light one and additional calculations on ensembles spanning a range of light quark masses. Higher statistics would be needed since statistical uncertainties will be larger than in this calculation, and the issue of topology freezing on fine lattices will be more significant. Our calculation demonstrates, however, that lattice QCD is no longer limited for these form factors by the systematic uncertainties coming from current matching and, with sufficient computer time, a 1% accurate result for $B \rightarrow D\ell\nu$ form factors is achievable.

ACKNOWLEDGMENTS

We are grateful to the MILC collaboration for the use of their configurations and their code. Computing was done on the Cambridge Service for Data Driven Discovery (CSD3) supercomputer, part of which is operated by the University of Cambridge Research Computing Service on behalf of the UK Science and Technology Facilities Council (STFC) DiRAC HPC Facility. The DiRAC component of CSD3 was funded by BEIS via STFC capital grants and is operated by STFC operations grants. We are grateful to the CSD3 support staff for assistance. Funding for this work came from STFC. We would also like to thank C. Bouchard, B. Colquhoun, D. Hatton, J. Harrison, P. Lepage and M. Wingate for useful discussions.

APPENDIX A: RECONSTRUCTING FORM FACTORS

This Appendix gives the necessary information to reproduce the functional form of the form factors through q^2 reproduced in this work. We here express the form factors in terms of the BCL parametrization [66]:

$$f_0^s(q^2) = \frac{1}{1 - \frac{q^2}{M_{B_{c0}}^2}} \sum_{n=0}^2 a_n^0 z^n(q^2),$$

$$f_+^s(q^2) = \frac{1}{1 - \frac{q^2}{M_{B_c^*}^2}} \sum_{n=0}^2 a_n^+ (z^n(q^2) - \frac{n}{3} (-1)^{n-3} z^3(q^2)), \quad (\text{A1})$$

where the function $z(q^2)$ is defined by

$$z(q^2) = \frac{\sqrt{t_+ - q^2} - \sqrt{t_+}}{\sqrt{t_+ - q^2} + \sqrt{t_+}}, \quad (\text{A2})$$

and $t_+ = (M_{B_s} + M_{D_s})^2$. We take the PDG 2018 values for these masses, 5.3669 GeV for the B_s and 1.9683 GeV for the D_s [28]. For the position of the poles, we use $M_{B_{c0}} = 6.704$ GeV and $M_{B_c^*} = 6.329$ GeV. The coefficients $a_n^{0,+}$ found from our fit, along with their covariance, is given in Table VIII.

TABLE VIII. Our results for z -coefficients in the BCL parametrization Eq. (A1). The first row gives mean values, and the rest of the table gives the covariance matrix associated with these parameters.

| a_0^0 | a_1^0 | a_2^0 | a_0^+ | a_1^+ | a_2^+ |
|---------|----------|----------|---------|----------|----------|
| 0.66574 | -0.25944 | -0.10636 | 0.66574 | -3.23599 | -0.07478 |
| 0.00015 | 0.00188 | 0.00070 | 0.00015 | 0.00022 | 0.00003 |
| | 0.06129 | 0.16556 | 0.00188 | 0.01449 | 0.00001 |
| | | 3.29493 | 0.00070 | 0.18757 | -0.00614 |
| | | | 0.00015 | 0.00022 | 0.00003 |
| | | | | 0.20443 | 0.10080 |
| | | | | | 4.04413 |

APPENDIX B: THE RATIO METHOD FOR OBTAINING THE FORM FACTORS

Here we show results from the *ratio* approach to determining the form factors. In this approach we fit the ratio of the form factors to decay constant of the pseudo-scalar H_c meson [49] [repeating the definition from Eq. (25)]:

$$R_{0,+}^s(q^2) \equiv \frac{f_{0,+}^s(q^2)}{f_{H_c} \sqrt{M_{H_c}}}. \quad (\text{B1})$$

Two-point correlation functions for the H_c meson are calculated along with the other two- and three-point correlation functions that we need (see Sec. II B) and included in the simultaneous fits to these correlation functions described in Sec. II C. This enables us to determine the heavy-charm meson decay constant [and in fact the combination $f_{H_c} \sqrt{M_{H_c}}$ needed for Eq. (B1)]

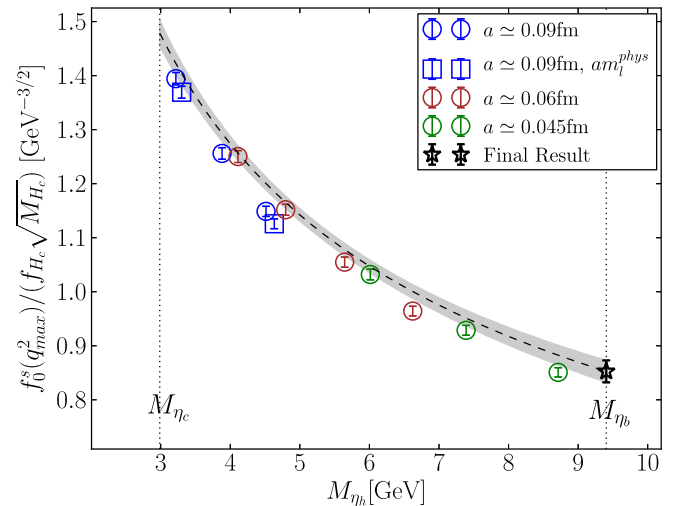


FIG. 16. $R_0^s(q_{\max}^2) = f_0^s(q_{\max}^2)/(f_{H_c} \sqrt{M_{H_c}})$ against M_{η_b} (a proxy for the heavy quark mass). The grey band shows the result of the extrapolation at $a = 0$ and physical l, s and c masses. Sets listed in the legend follow the order of sets in Table I.

TABLE IX. Error budget for $R_0^s(q_{\max}^2)$.

| Source | % Fractional error |
|---|--------------------|
| Statistics | 1.10 |
| Scale setting | 1.30 |
| $m_h \rightarrow m_b$ and $a \rightarrow 0$ | 1.44 |
| Quark mistuning | 0.87 |
| Total | 2.39 |

from the amplitude for the ground-state in the two-point correlation functions as given in Eq. (21). Our results for $R_{0,+}^s(q^2)$ are given in Table IV.

We fit $R_{0,+}^s(q^2)$ using an identical fit function to that of the direct approach, given in Eqs. (26) and (28). The fit parameters are tabulated in Table XI in Appendix C. Discretization effects change in the ratio given in Eq. (B1), compared to those from the form factors themselves, changing the continuum extrapolation. The dependence on heavy quark mass of the ratio is also very different. The value of the ratio at the physical point (where $m_h = m_b$ and $a = 0$) can then multiplied by $f_{B_c} \sqrt{M_{B_c}}$ to obtain the form factors. We find f_{B_c} via a separate calculation (detailed in Appendix A of [49]) and take the experimental value for the B_c meson mass, $M_{B_c} = 6.2756(11)$ GeV [28]. This approach has the disadvantage of introducing larger uncertainties from scale-setting since $R_{0,+}^s(q^2)$ are dimensionful quantities (as opposed to $f_{0,+}^s(q^2)$ which are dimensionless). Hence we do not use it for our final value. It provides a useful test of our uncertainties, however.

1. Zero recoil

We first show results from a fit at the zero recoil point, $R_0^s(q_{\max}^2)$, as a function of heavy quark mass and lattice spacing. To do this we use the same fit form as for our fits to

$f_{0,+}^s(q_{\max}^2)$, given in Eq. (32), with the same priors. We find, with physical parameters for all quark masses and $a = 0$

$$R_0^s(q_{\max}^2) = \frac{f_0^s(q_{\max}^2)}{f_{B_c} \sqrt{M_{B_c}}} = 0.853(20) \text{ GeV}^{-3/2}. \quad (\text{B2})$$

The fit has $\chi^2/N_{\text{dof}} = 0.63$ for $N_{\text{dof}} = 16$. The lattice QCD results and fit are shown in a plot against M_{η_h} in Fig. 16. As can be seen from this plot, the lattice results have stronger dependence on the heavy quark mass and somewhat less on the lattice spacing compared to that seen in Fig. 4. The error budget for our physical value in Eq. (B2) is given in Table IX. Notice that, compared to Table VI it now has a significant scale-setting uncertainty.

2. Full q^2 range

In Fig. 17, we show the complete set of lattice results along with the results of the full fit given by the fit form in Eq. (28). As for Fig. 7 we see that as the lattice spacing decreases, the range of heavy quark masses increases and the q^2 range, $0 < (M_{H_s} - M_{D_s})^2$ expands. The goodness of fit here was $\chi^2/N_{\text{dof}} = 0.57$, $N_{\text{dof}} = 58$.

To obtain the form factors, the resulting functions $R_{0,+}^s(q^2)$ were multiplied by $\sqrt{M_{B_c}}$ (using the experimental value) and f_{B_c} from our determination detailed in Appendix A of [49]. The resulting form factors are shown in Figure 10 in a comparison to those found by our direct method of Sec. III B.

APPENDIX C: FIT OUTPUTS

Here we give the results for the free parameters from our fit described in Sec. II E, with Eqs. (28) and (29). Most of the parameters in these equations are not well determined by the fit. The point of including them in the fit is then to make sure that the uncertainty from not knowing them is

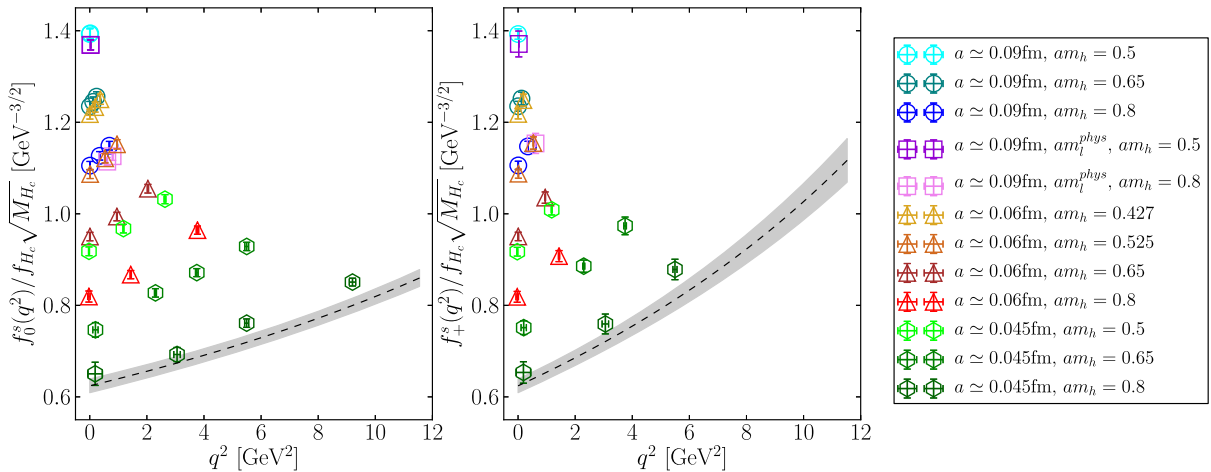


FIG. 17. $R_{0,+}^s(q^2) = f_{0,+}^s(q^2)/(f_{H_c} \sqrt{M_{H_c}})$ plotted against q^2 . The grey band shows the result of our fit at $a = 0$ and physical l, s, c and b masses. Sets listed in the legend follow the order of sets in Table I.

TABLE X. Fit results for the parameters d_{ijkn}^0 , d_{ijkn}^+ , ρ_n^0 and ρ_n^+ defined in Eq. (28) and used in our preferred fit described in Sec. II E. We give the mean values and uncertainties, but do not include the correlation matrix. The $n = 0$ parameters for $j = k = 0$ are the same for d^0 and d^+ , as are the $n = 0$ parameters for ρ^0 and ρ^+ . We restrict the list to those parameters that are constrained by the fit beyond the prior value of 0 ± 2 , but include values that are not constrained for $n = 1$ where the $n = 0$ result is constrained. $n = 2$ parameters are also included in the fit but they are not constrained.

| i, j, k | d^0 | | d^+ | |
|-----------|-----------|------------|-----------|-------------|
| | $n = 0$ | $n = 1$ | $n = 0$ | $n = 1$ |
| 0,0,0 | 1.397(82) | -0.25(33) | 1.397(82) | -3.45(87) |
| 1,0,0 | -1.01(49) | 0.4(1.5) | -1.01(49) | -1.0(1.9) |
| 2,0,0 | -0.62(77) | 0.1(2.0) | -0.62(77) | -0.3(2.0) |
| 0,1,0 | 0.29(33) | 0.9(1.6) | 0.30(32) | -0.1(2.0) |
| 1,1,0 | 0.4(1.6) | 0.2(2.0) | 0.4(1.6) | -0.04(2.00) |
| 0,2,0 | 1.4(1.4) | 0.06(2.00) | 1.3(1.4) | 0.0(2.0) |
| 0,0,1 | -0.16(91) | 0.2(2.0) | -0.14(91) | -0.06(2.00) |
| 1,0,1 | -0.2(1.7) | 0.05(2.00) | -0.2(1.7) | -0.01(2.00) |
| | ρ^0 | | ρ^+ | |
| | 0.419(20) | -0.23(96) | 0.419(20) | 0.08(25) |

fed into our final results. In these cases the fit simply returns the prior value for that parameter, and we do not list these.

The parameters that can be determined from the fit are mainly those associated with the leading $n = 0$ coefficient in the z -expansion. Some information about the $n = 1$ term is also obtained, but none of the $n = 2$ coefficients are constrained. Table X gives the mean values and uncertainties of the coefficients d_{ijkn}^0 and d_{ijkn}^+ from

TABLE XI. Fit results for the parameters d_{ijkn}^0 , d_{ijkn}^+ , ρ_n^0 and ρ_n^+ defined in Eq. (28) but used with the alternative ratio fit described in Appendix B. We give the mean values and uncertainties, but do not include the correlation matrix. The $n = 0$ parameters for $j = k = 0$ are the same for d^0 and d^+ , as are the $n = 0$ parameters for ρ^0 and ρ^+ . We restrict the list to those parameters that are constrained by the fit beyond the prior value of 0 ± 2 , but include values that are not constrained for $n = 1$ where the $n = 0$ result is constrained. $n = 2$ parameters are also included in the fit but they are not constrained.

| i, j, k | d^0 | | d^+ | |
|-----------|------------|------------|-------------|-------------|
| | $n = 0$ | $n = 1$ | $n = 0$ | $n = 1$ |
| 0,0,0 | 1.12(13) | -0.28(36) | 1.12(13) | -3.93(98) |
| 1,0,0 | 1.93(75) | 0.5(1.6) | 1.93(75) | -1.1(1.9) |
| 2,0,0 | -2.6(1.1) | 0.1(2.0) | -2.6(1.1) | -0.3(2.0) |
| 0,1,0 | 0.88(40) | 0.2(1.8) | -0.82(50) | -0.03(1.99) |
| 1,1,0 | -0.5(1.8) | 0.1(2.0) | 0.3(1.8) | -0.02(2.00) |
| 0,2,0 | 0.02(1.82) | 0.02(2.00) | -0.04(1.86) | 0.0(2.0) |
| 0,0,1 | -0.5(1.1) | 0.2(2.0) | -0.34(69) | -0.2(2.0) |
| 1,0,1 | -0.4(1.9) | 0.04(2.00) | 0.3(1.6) | -0.05(2.00) |
| | ρ^0 | | ρ^+ | |
| | 0.452(27) | -0.21(93) | 0.452(27) | 0.26(21) |

Eq. (28) for $n = 0$ and $n = 1$ that are constrained from the fit. The d^+ coefficients for $n = 0$ and $j = k = 0$ are the same as those for d^0 , to implement the constraint that $f_+(0) = f_0(0)$. The values of the ρ parameters obtained for $n = 0$ and $n = 1$ ($n = 2$ is not constrained) are also given in Table X. For $n = 0$ $\rho_0^0 = \rho_0^+$, again to enforce $f_0(0) = f_+(0)$. The mass mistuning parameters given in Eq. (29) are not constrained by the fit.

Table XI gives the same information for the alternative ratio fit described in Appendix B.

APPENDIX D: TESTS OF UNITARITY BOUNDS

Unitarity and crossing symmetry imposes bounds on the coefficients of the BCL parametrization of $f_{0,+}(q^2)$, $\{a_n\}$ [75,76]. As another consistency test, we show here that the coefficients for f_+ found in our fit satisfy these bounds.

To obtain bounds on the BCL coefficients [66], one must relate them to those of a different parametrization, that of Boyd, Grinstein and Lebed (BGL) [77]:

$$f_+^s(q^2) = \frac{1}{B(z)\phi(z)} \sum_{n \geq 0}^N b_n z^n. \quad (D1)$$

$B(z)$ is known as the Blaschke factor:

$$B(z) = \frac{z - z_*}{1 - z z_*}, \quad (D2)$$

where $z_* = z(M_{B_s}^2)$ for f_+^s . $\phi(z)$ is the outer function;

$$\begin{aligned} \phi(z) &= M_{B_s}^{2-s} 2^{2+p} \sqrt{\kappa n_f} \left[\frac{M_{D_s}}{M_{B_s}} (1+z) \right]^{s-3/2} \\ &\times \left[(1-z) \left(1 + \frac{M_{D_s}}{M_{B_s}} \right) + 2 \sqrt{\frac{M_{D_s}}{M_{B_s}}} (1+z) \right]^{-s-p}. \end{aligned} \quad (D3)$$

In the f_+^s case, $\kappa = 6\pi M_{B_s}^2 \chi_V$, $p = 3$, $s = 2$. The quantity χ_V is the once-subtracted dispersion relation at $q^2 = 0$ for the vector $b \rightarrow c$ current, computed in [77] to be $\chi_V = 5.7 \times 10^{-3}/m_b^2$.

The BGL coefficients, $\{b_n\}$, obey the unitarity constraint

$$\sum_{m=0}^{\infty} |b_m|^2 \leq 1 \quad (D4)$$

by construction of the parametrization. To see how this applies to the BCL coefficients $\{a_n\}$, one must relate them to $\{b_m\}$ by equating the two parametrizations to find [66]

$$\sum_{m=0}^M b_m z^m = \psi(z) \sum_{n=0}^N a_n z^n, \quad (D5)$$

where $\psi(z)$ is given by

$$\psi(z) = \frac{M_{\text{pole}}^2}{4(t_+ - t_0)} \phi(z) \frac{(1-z)^2(1-z_*)^2}{(1-zz_*)^2}, \quad (\text{D6})$$

and $M_{\text{pole}} = M_{B_c^*}$ in the f_+^s case. Expanding $\psi(z)$ around $z = 0$, comparing coefficients of z in Eq. (D5), and imposing the constraint of Eq. (D4), we arrive at a constraint for the BCL coefficients

$$\mathcal{B} \equiv \sum_{j,k=0}^{L,L} B_{jk} a_j a_k \leq 1, \quad (\text{D7})$$

$$B_{jk} = \sum_{n=0}^{\infty} \eta_n \eta_{n+|j-k|}, \quad (\text{D8})$$

where $\{\eta_n\}$ are the Taylor coefficients of $\psi(z)$.

$\psi(z)$ is bounded on the closed disk $|z| < 1$, so its Taylor coefficients are rapidly decreasing. We computed values for B_{jk} by truncating the sum in its definition [Eq. (D8)] at 100.

TABLE XII. Numerical values for B_{jk} appearing in the unitarity bound for BCL coefficients, defined in (D8), for the f_+^s case. The rest of the elements can be obtained from these using the properties $B_{j(j+k)} = B_{0k}$ and $B_{jk} = B_{kj}$.

| | B_{00} | B_{01} | B_{02} |
|---------|----------|-----------|----------|
| f_+^s | 0.00179 | -0.000367 | 0.00108 |

These values are given in Table XII. With these B_{jk} values, and the a_n coefficients from our fit (via the direct method), we find

$$\mathcal{B}_+ = 0.0210(54).$$

This comfortably satisfies the unitarity bound. Additionally, as discussed in [78], the leading contributions to \mathcal{B}_+ are of order $(\Lambda_{\text{QCD}}/m_b)^3 \simeq 10^{-3}$ in the heavy quark expansion. This expectation is approximately fulfilled by our result.

-
- [1] J. T. Wei *et al.* (Belle Collaboration), *Phys. Rev. Lett.* **103**, 171801 (2009).
 - [2] J. P. Lees *et al.* (BABAR Collaboration), *Phys. Rev. Lett.* **109**, 101802 (2012).
 - [3] J. P. Lees *et al.* (BABAR Collaboration), *Phys. Rev. D* **86**, 032012 (2012).
 - [4] J. P. Lees *et al.* (BABAR Collaboration), *Phys. Rev. D* **88**, 072012 (2013).
 - [5] R. Aaij *et al.* (LHCb Collaboration), *J. High Energy Phys.* **06** (2014) 133.
 - [6] R. Aaij *et al.* (LHCb Collaboration), *Phys. Rev. Lett.* **113**, 151601 (2014).
 - [7] M. Huschle *et al.* (Belle Collaboration), *Phys. Rev. D* **92**, 072014 (2015).
 - [8] R. Aaij *et al.* (LHCb Collaboration), *J. High Energy Phys.* **02** (2016) 104.
 - [9] R. Aaij *et al.* (LHCb Collaboration), *Phys. Rev. Lett.* **115**, 111803 (2015); **115**, 159901(E) (2015).
 - [10] R. Aaij *et al.* (LHCb Collaboration), *J. High Energy Phys.* **06** (2015) 115; **09** (2018) 145(E).
 - [11] R. Aaij *et al.* (LHCb Collaboration), *J. High Energy Phys.* **11** (2016) 047; **04** (2017) 142(E).
 - [12] S. Wehle *et al.* (Belle Collaboration), *Phys. Rev. Lett.* **118**, 111801 (2017).
 - [13] Y. Sato *et al.* (Belle Collaboration), *Phys. Rev. D* **94**, 072007 (2016).
 - [14] S. Hirose *et al.* (Belle Collaboration), *Phys. Rev. D* **97**, 012004 (2018).
 - [15] R. Aaij *et al.* (LHCb Collaboration), *Phys. Rev. D* **97**, 072013 (2018).
 - [16] R. Aaij *et al.* (LHCb Collaboration), *Phys. Rev. Lett.* **120**, 171802 (2018).
 - [17] R. Aaij *et al.* (LHCb Collaboration), *J. High Energy Phys.* **08** (2017) 055.
 - [18] A. M. Sirunyan *et al.* (CMS Collaboration), *Phys. Lett. B* **781**, 517 (2018).
 - [19] M. Aaboud *et al.* (ATLAS Collaboration), *J. High Energy Phys.* **10** (2018) 047.
 - [20] B. Aubert *et al.* (BABAR Collaboration), *Phys. Rev. D* **79**, 012002 (2009).
 - [21] B. Aubert *et al.* (BABAR Collaboration), *Phys. Rev. Lett.* **104**, 011802 (2010).
 - [22] J. A. Bailey *et al.* (MILC Collaboration), *Phys. Rev. D* **92**, 034506 (2015).
 - [23] H. Na, C. M. Bouchard, G. P. Lepage, C. Monahan, and J. Shigemitsu (HPQCD Collaboration), *Phys. Rev. D* **92**, 054510 (2015); **93**, 119906(E) (2016).
 - [24] R. Glattauer *et al.* (Belle Collaboration), *Phys. Rev. D* **93**, 032006 (2016).
 - [25] F. U. Bernlochner, Z. Ligeti, M. Papucci, and D. J. Robinson, *Phys. Rev. D* **95**, 115008 (2017); **97**, 059902(E) (2018).
 - [26] D. Bigi, P. Gambino, and S. Schacht, *Phys. Lett. B* **769**, 441 (2017).
 - [27] B. Grinstein and A. Kobach, *Phys. Lett. B* **771**, 359 (2017).
 - [28] M. Tanabashi *et al.* (Particle Data Group), *Phys. Rev. D* **98**, 030001 (2018).
 - [29] J. P. Lees *et al.* (BABAR Collaboration), *Phys. Rev. Lett.* **123**, 091801 (2019).

- [30] P. Gambino, M. Jung, and S. Schacht, *Phys. Lett. B* **795**, 386 (2019).
- [31] J. Koponen, C. T. H. Davies, G. C. Donald, E. Follana, G. P. Lepage, H. Na, and J. Shigemitsu (HPQCD Collaboration), [arXiv:1305.1462](https://arxiv.org/abs/1305.1462).
- [32] E. McLean, C. T. H. Davies, A. T. Lytle, and J. Koponen (HPQCD Collaboration), *Proc. Sci., LATTICE2018* (2019) 281 [[arXiv:1901.04979](https://arxiv.org/abs/1901.04979)].
- [33] J. Laiho and R. S. Van de Water, *Phys. Rev. D* **73**, 054501 (2006).
- [34] J. A. Bailey *et al.* (Fermilab/MILC Collaboration), *Phys. Rev. D* **85**, 114502 (2012); **86**, 039904(E) (2012).
- [35] C. J. Monahan, H. Na, C. M. Bouchard, G. P. Lepage, and J. Shigemitsu (HPQCD Collaboration), *Phys. Rev. D* **95**, 114506 (2017).
- [36] Y. Amhis *et al.* (HFLAV Collaboration), *Eur. Phys. J. C* **77**, 895 (2017).
- [37] G. Caria (Belle Collaboration), Measurement of $R(D)$ and $R(D^*)$ with a semileptonic tag at Belle, *54th Rencontres de Moriond on Electroweak Interactions, La Thuile, Italy* (2019), [arXiv:1910.05864](https://arxiv.org/abs/1910.05864).
- [38] M. Atoui, V. Morénas, D. Bečirevic, and F. Sanfilippo, *Eur. Phys. J. C* **74**, 2861 (2014).
- [39] J. M. Flynn, R. C. Hill, A. Jüttner, A. Soni, J. T. Tsang, and O. Witzel, *Proc. Sci., LATTICE2018* (2019) 290.
- [40] E. Follana, Q. Mason, C. Davies, K. Hornbostel, G. P. Lepage, J. Shigemitsu, H. Trotter, and K. Wong (HPQCD and UKQCD Collaborations), *Phys. Rev. D* **75**, 054502 (2007).
- [41] A. Bazavov *et al.* (MILC Collaboration), *Phys. Rev. D* **87**, 054505 (2013).
- [42] C. McNeile, C. T. H. Davies, E. Follana, K. Hornbostel, and G. P. Lepage, *Phys. Rev. D* **82**, 034512 (2010).
- [43] C. McNeile, C. T. H. Davies, E. Follana, K. Hornbostel, and G. P. Lepage (HPQCD Collaboration), *Phys. Rev. D* **85**, 031503 (2012).
- [44] C. McNeile, C. T. H. Davies, E. Follana, K. Hornbostel, and G. P. Lepage, *Phys. Rev. D* **86**, 074503 (2012).
- [45] A. Bazavov *et al.* (Fermilab/MILC Collaboration), *Phys. Rev. D* **98**, 074512 (2018).
- [46] P. Petreczky and J. H. Weber, *Phys. Rev. D* **100**, 034519 (2019).
- [47] A. Lytle, B. Colquhoun, C. Davies, J. Koponen, and C. McNeile (HPQCD Collaboration), *Proc. Sci., BEAUTY2016* (2016) 069 [[arXiv:1605.05645](https://arxiv.org/abs/1605.05645)].
- [48] B. Colquhoun, C. Davies, J. Koponen, A. Lytle, and C. McNeile (HPQCD Collaboration), *Proc. Sci., LATTICE2016* (2016) 281 [[arXiv:1611.01987](https://arxiv.org/abs/1611.01987)].
- [49] E. McLean, C. T. H. Davies, A. T. Lytle, and J. Koponen, *Phys. Rev. D* **99**, 114512 (2019).
- [50] A. Bazavov *et al.* (MILC Collaboration), *Phys. Rev. D* **82**, 074501 (2010).
- [51] A. Hart, G. M. von Hippel, and R. R. Horgan (HPQCD Collaboration), *Phys. Rev. D* **79**, 074008 (2009).
- [52] S. Borsanyi *et al.*, *J. High Energy Phys.* 09 (2012) 010.
- [53] R. J. Dowdall, C. T. H. Davies, G. P. Lepage, and C. McNeile (HPQCD Collaboration), *Phys. Rev. D* **88**, 074504 (2013).
- [54] B. Chakraborty, C. T. H. Davies, B. Galloway, P. Knecht, J. Koponen, G. C. Donald, R. J. Dowdall, G. P. Lepage, and C. McNeile (HPQCD Collaboration), *Phys. Rev. D* **91**, 054508 (2015).
- [55] B. Chakraborty, C. T. H. Davies, P. G. de Oliveira, J. Koponen, G. P. Lepage, and R. S. Van de Water (HPQCD Collaboration), *Phys. Rev. D* **96**, 034516 (2017).
- [56] C. McNeile (private communication).
- [57] C. T. H. Davies, C. McNeile, E. Follana, G. P. Lepage, H. Na, and J. Shigemitsu (HPQCD Collaboration), *Phys. Rev. D* **82**, 114504 (2010).
- [58] D. Guadagnoli, F. Mescia, and S. Simula, *Phys. Rev. D* **73**, 114504 (2006).
- [59] C. T. H. Davies, E. Follana, I. D. Kendall, G. P. Lepage, and C. McNeile (HPQCD Collaboration), *Phys. Rev. D* **81**, 034506 (2010).
- [60] G. P. Lepage, B. Clark, C. T. H. Davies, K. Hornbostel, P. B. Mackenzie, C. Morningstar, and H. Trotter, *Nucl. Phys. B, Proc. Suppl.* **106**, 12 (2002).
- [61] Corrfitter, <https://github.com/gplepage/corrfitter> (2018).
- [62] R. J. Dowdall, C. T. H. Davies, R. R. Horgan, G. P. Lepage, C. J. Monahan, J. Shigemitsu, and M. Wingate, *Phys. Rev. D* **100**, 094508 (2019).
- [63] G. C. Donald, C. T. H. Davies, R. J. Dowdall, E. Follana, K. Hornbostel, J. Koponen, G. P. Lepage, and C. McNeile, *Phys. Rev. D* **86**, 094501 (2012).
- [64] G. C. Donald, C. T. H. Davies, J. Koponen, and G. P. Lepage (HPQCD Collaboration), *Phys. Rev. D* **90**, 074506 (2014).
- [65] C. Monahan, J. Shigemitsu, and R. Horgan, *Phys. Rev. D* **87**, 034017 (2013).
- [66] C. Bourrely, I. Caprini, and L. Lellouch, *Phys. Rev. D* **79**, 013008 (2009); **82**, 099902(E) (2010).
- [67] R. J. Dowdall, C. T. H. Davies, T. C. Hammant, and R. R. Horgan, *Phys. Rev. D* **86**, 094510 (2012).
- [68] C. Bernard and D. Toussaint (MILC Collaboration), *Phys. Rev. D* **97**, 074502 (2018).
- [69] A. Bazavov *et al.* (Fermilab Lattice and MILC Collaboration), *Phys. Rev. D* **100**, 034501 (2019).
- [70] I. Caprini, L. Lellouch, and M. Neubert, *Nucl. Phys.* **B530**, 153 (1998).
- [71] D. Bigi, P. Gambino, and S. Schacht, *J. High Energy Phys.* 11 (2017) 061.
- [72] T. Kaneko, Y. Aoki, B. Colquhoun, H. Fukaya, and S. Hashimoto (JLQCD Collaboration), *Proc. Sci., LATTICE2018* (2018) 311.
- [73] R. J. Hill, *Phys. Rev. D* **73**, 014012 (2006).
- [74] R. J. Hill, *eConf* **C060409**, 027 (2006).
- [75] S. Okubo, *Phys. Rev. D* **4**, 725 (1971).
- [76] S. Okubo, *Phys. Rev. D* **3**, 2807 (1971).
- [77] C. G. Boyd, B. Grinstein, and R. F. Lebed, *Nucl. Phys.* **B461**, 493 (1996).
- [78] T. Becher and R. J. Hill, *Phys. Lett. B* **633**, 61 (2006).